

NOV 29



High Resolution Measurements of Supersonic Shear Flow Mixing and Combustion

Werner J.A. Dahm and James F. Driscoll

Final Report No. 036407 – 3
AFOSR Contract F49620-98-1-0003

Laboratory for Turbulence and Combustion (LTC)

www.engin.umich.edu/dept/aero/ltc

Department of Aerospace Engineering
The University of Michigan
Ann Arbor, MI 48109-2140

DISTRIBUTION STATEMENT A
Approved for Public Release
Distribution Unlimited

October 2001

20020107 112

REPORT DOCUMENTATION PAGE

Public reporting burden for this collection of information is estimated to average 1 hour per response, including the time for reviewing instructions, data needed, and completing and reviewing this collection of information. Send comments regarding this burden estimate or any other aspect of this burden to Department of Defense, Washington Headquarters Services, Directorate for Information Operations and Reports (0704-014302). Respondents should be aware that notwithstanding any other provision of law, no person shall be subject to any penalty for failing to comply with a valid OMB control number. PLEASE DO NOT RETURN YOUR FORM TO THE ABOVE ADDRESS.

AFRL-SR-BL-TR-01-

0656

ly

1. REPORT DATE (DD-MM-YYYY) 18-09-2001			2. REPORT TYPE Final Technical		3. DATES COVERED (From - To) 01-10-1997 - 30-09-2000	
4. TITLE AND SUBTITLE (U) High Resolution Measurements of Supersonic Shear Flow Mixing and Combustion					5a. CONTRACT NUMBER	
					5b. GRANT NUMBER F49620-98-1-0003	
					5c. PROGRAM ELEMENT NUMBER 61102F	
6. AUTHOR(S) Werner J. A. Dahm and James F. Driscoll					5d. PROJECT NUMBER 2308	
					5e. TASK NUMBER BX	
					5f. WORK UNIT NUMBER	
7. PERFORMING ORGANIZATION NAME(S) AND ADDRESS(ES) University of Michigan Ann Arbor MI 48109-2140					8. PERFORMING ORGANIZATION REPORT NUMBER	
9. SPONSORING / MONITORING AGENCY NAME(S) AND ADDRESS(ES) AFOSR/NA 801 North Randolph Street Room 732 Arlington VA 22203-1977					10. SPONSOR/MONITOR'S ACRONYM(S)	
					11. SPONSOR/MONITOR'S REPORT NUMBER(S)	
12. DISTRIBUTION / AVAILABILITY STATEMENT Approved for public release; distribution is unlimited					AIR FORCE OFFICE OF SCIENTIFIC RESEARCH (AFOSR) NOTICE OF TRANSMITTAL DTIC. THIS TECHNICAL REPORT HAS BEEN REVIEWED AND IS APPROVED FOR PUBLIC RELEASE LAW AFR 190-12. DISTRIBUTION IS UNLIMITED.	
13. SUPPLEMENTARY NOTES						
14. ABSTRACT An experimental investigation of compressibility effects on the large-scale structure, scaling laws, and entrainment and mixing rates in supersonic, planar, turbulent, bluff-body wakes was conducted. The compressibility effects in supersonic wakes were found to differ significantly from those in supersonic mixing layers. Results at free stream Mach numbers 2 and 3 showed that the large-scale structure of incompressible turbulent wakes was recovered in supersonic wakes at downstream locations where the local Mach number became sufficiently small. No organized large-scale structure was found where the local Mach number was greater than 0.7. Unlike supersonic mixing layers, the results showed that the principal effect of compressibility in supersonic wakes was a local self-induced forcing, where reflected expansion waves from the near-field recompression region intersected the wake.						
15. SUBJECT TERMS supersonic combustion, turbulent combustion, shear flows, flames						
16. SECURITY CLASSIFICATION OF:			17. LIMITATION OF ABSTRACT	18. NUMBER OF PAGES	19a. NAME OF RESPONSIBLE PERSON Julian M. Tishkoff	
a. REPORT Unclassified	b. ABSTRACT Unclassified	c. THIS PAGE Unclassified	UL	78	19b. TELEPHONE NUMBER (include area code) (703) 696-8478	



High Resolution Measurements of Supersonic Shear Flow Mixing and Combustion

Werner J.A. Dahm and James F. Driscoll

Final Report No. 036407 – 3
AFOSR Contract F49620-98-1-0003

Laboratory for Turbulence and Combustion (LTC)

www.engin.umich.edu/dept/aero/ltc

Department of Aerospace Engineering
The University of Michigan
Ann Arbor, MI 48109-2140

October 2001

Executive Summary

Previous investigations of compressibility effects in supersonic turbulent shear flows have focused largely on supersonic mixing layers, and have shown large reductions in the entrainment and mixing rate with increasing compressibility. The present study provides corresponding results for supersonic, planar, turbulent, bluff-body wakes to clarify the generic effects of compressibility in turbulent shear flows. Experiments using planar laser Mie scattering, shadowgraphy, and pressure surveys investigated the large-scale structure, mean velocity fields, and scaling properties of $M_\infty \approx 2$ and $M_\infty \approx 3$ wakes, and compared these with corresponding results from incompressible wakes. Results show that the large-scale structure of incompressible planar turbulent wakes is recovered in supersonic wakes at downstream locations x where the local relative Mach number $M_r(x)$ has become sufficiently small. No comparable organized large-scale structure is evident where the relative Mach number is large. However, unlike supersonic mixing layers or slender-body wakes, the present results show the principal effect of compressibility in supersonic bluff-body wakes to be a local self-induced forcing that occurs where the reflected expansion waves from the near-field recompression region intersect the wake. The $M_\infty \approx 2$ wake permits a subsonic upstream path from this intersection point, and the local wave-induced forcing therefore alters the wake scaling constants to match those obtained in forced incompressible wakes. In the $M_\infty \approx 3$ wake, no subsonic upstream path exists from the intersection point, and the scaling constants match the values found in unforced incompressible wakes. Downstream of each intersection point, the interaction leads to a dramatic increase in the wake growth rate and an attendant local increase in the entrainment rate, however the wake subsequently detrains this fluid and returns to its original growth rate. The compressibility effects in supersonic bluff-body turbulent wakes are thus seen to be significantly different from those in supersonic mixing layers.

This Final Report summarizes several major findings from an experimental and theoretical investigation of entrainment and mixing in supersonic turbulent shear flows. In addition, a number of archival publications have resulted, in part or in whole, from the work done under this AFOSR contract. These are summarized below, and can be consulted for additional details on any of the sections of the present report.

1. Nakagawa, M. and Dahm, W.J.A. (1999) Compressibility effects on entrainment and mixing in supersonic planar turbulent wakes. AIAA Paper No. 99-3582, 30th AIAA Fluid Dynamics Conference, June 28 - July 1, 1999, Norfolk, VA.
2. Nakagawa, M. and Dahm, W.J.A. (2000) Experimental results on the near-field

structure of supersonic planar turbulent wakes. AIAA Paper No. 2000-0664, 38th AIAA Aerospace Sciences Meeting, January 10 - 13, 2000, Reno, NV.

3. Nakagawa, M. and Dahm, W.J.A. (2000) Velocity measurements in the near-field of supersonic planar turbulent wakes. AIAA Paper No. 2000-2468, AIAA Fluids 2000 Fluid Dynamics Meeting, June, 2000, Boulder, CO.
4. Nakagawa, M. and Dahm, W.J.A. (2000) Control of entrainment and mixing in supersonic turbulent shear flows by expansion wave interactions. Proc. EUROMECH Colloquium 415 on Shear Flow Control, July 24 - 26, 2000, TU Berlin, Germany.
5. Nakagawa, M. and Dahm, W.J.A. (2001) Experimental study of entrainment and mixing in supersonic planar turbulent wakes. Part 1. Far-field scaling properties and effects of wave interaction. Submitted to Journal of Fluid Mechanics.
6. Nakagawa, M. and Dahm, W.J.A. (2001) Experimental study of entrainment and mixing in supersonic planar turbulent wakes. Part 2. Large-scale structure and comparisons with incompressible wakes. In preparation for Journal of Fluid Mechanics.
5. Nakagawa, M. (2001) Experimental study of entrainment and mixing in supersonic planar turbulent wakes. Ph.D. Thesis, Department of Aerospace Engineering, The University of Michigan, Ann Arbor.
8. Tacina, K.M. and Dahm, W.J.A. (1999) An equivalence principle for heat release effects in nonbuoyant turbulent shear flows and its application to turbulent jet flames. Proc. 1999 Joint Technical Meeting of the U.S. Sections of the Combustion Institute, pp. 344-347, Washington, D.C., March 14-17, 1999, The Combustion Institute, Pittsburgh.
9. Tacina, K.M. and Dahm, W.J.A. (2000) Effects of heat release on turbulent shear flows. Part 1. A general equivalence principle for nonbuoyant flows and its application to turbulent jet flames. Journal of Fluid Mechanics, Vol. 415, pp. 23 - 44.
10. Dahm, W.J.A. (2000) Effects of heat release on turbulent shear flows. Part 2. Turbulent mixing layers. In preparation for Journal of Fluid Mechanics.
11. Burton, G.C., Dahm, W.J.A., Dowling, D.R. and Powell, K.G. (2000) Multifractal scale-similarity in subgrid-scale turbulence modeling. Proc. EUROMECH 8th European Turbulence Conference (ETC8), June 27-30, 2000, Barcelona, Spain.
12. Mullin, J.A. and Dahm, W.J.A. (2000) Combined PLIF and PIV laser imaging measurements of heat release effects at the small scales of turbulent reacting flows. Proc. 10th International Symposium on Application of Laser Techniques to Fluid Mechanics, July 10-13, 2000, Lisbon, Portugal.
13. Donbar, J.M., Carter, C.D., Ratner, A., Driscoll, J.F. and Dahm, W.J.A. (1998) Simultaneous velocity-scalar measurements within intensely wrinkled nonpremixed

flames. Proc. Western States Section Meeting of the Combustion Institute, Paper 98F-37, Seattle, WA October 26-27, 1998; The Combustion Institute, Pittsburgh.

14. Ratner, A., Donbar, J.M., Carter, C.D., Driscoll J.F. and Dahm, W.J.A. (1999) The regime of intensely wrinkled nonpremixed flames – Images of the CH-OH reaction zones and velocity fields. Proc. 1999 Joint Technical Meeting of the U.S. Sections of the Combustion Institute, Washington, D.C., March 14-17, 1999, The Combustion Institute, Pittsburgh.
15. Ratner, A., Driscoll J.F., Donbar, J.M., Carter, C.D., Mullin, J.A. and Dahm, W.J.A. (1999) The new regime of intensely wrinkled and shredded nonpremixed flames – Images of the reaction zone; Proc. Eastern States Section Meeting of the Combustion Institute, Raleigh-Durham, N.C., October 11-13, 1999, The Combustion Institute, Pittsburgh.
16. Dahm, W.J.A. and Southerland, K.B. (1999) Quantitative flow visualization via fully-resolved four-dimensional spatio-temporal imaging. Chapter 11 in Flow Visualization: Techniques and Examples, (A. Smits and T.T. Lim, Eds.), 231 – 258, Imperial College Press, London.
17. Dahm, W.J.A., Tryggvason, G., Frederiksen, R.D. and Stock, M.J. (2000) Local integral moment (LIM) simulations. Chapter 5 in Computational Fluid Dynamics in Industrial Combustion, pp. 161 – 208, (C.M. Baukal, Ed.), CRC Press

1. Technical Background

Future airbreathing propulsion systems will likely involve supersonic combustors, in which a subsonic fuel stream must be mixed and burned with a supersonic airstream. Under such conditions, compressibility effects can significantly alter the entrainment and mixing processes from prior experience in subsonic flows. Understanding the effects of compressibility on supersonic turbulent shear flows is therefore a key to successful development of the next generation of high-speed airbreathing propulsion systems. For this reason, research over the past fifteen years has sought to develop a fundamental understanding of the generic effects of compressibility on entrainment and mixing in supersonic turbulent shear flows by studying elementary flows under carefully controlled conditions.

Certain insights relevant to entrainment and mixing processes in turbulent shear flows can be obtained from elementary scaling considerations alone. Following classical theory, free stream fluid is entrained into any shear-driven turbulent flow at an initial length scale proportional to δ , where $\delta(x)$ and $u(x)$ are the local “outer” length and velocity scales that characterize the local mean shear in the flow that drives the turbulence at any downstream location x . In the subsequent equilibrium turbulent cascade process, the repeated stretching and folding action of the strain rate and vorticity fields reduces the length scales of this entrained fluid from the initial scale $\delta(x)$ to the smallest local “inner” length scale $\lambda_v \sim \delta \cdot Re_\delta^{-3/4}$, which is set by the effects of viscous diffusion. Here $Re_\delta \equiv u(x) \delta(x)/\nu$ is the local outer-scale Reynolds number, with ν the kinematic viscosity. This turbulent cascade process requires a time of the order of the local outer time scale $\tau_\delta \sim \delta(x)/u(x)$ to reach the inner length scale λ_v . Further mixing by molecular diffusion from this inner length scale to the molecular scale needed for chemical reaction requires a time of the order of the diffusive time scale $\tau_v \sim (\lambda_v^2/\nu)$. Completion of the chemical reactions involved in combustion requires a time of the order of the characteristic reaction time scale $\tau_k \sim (1/k)$, where k is the overall reaction rate. The ratios of these three time scales then characterizes the relative rates of each of the three steps in the combined entrainment, mixing, and chemical reaction process. In particular, the

reaction-to-diffusion time scale ratio $\tau_r/\tau_v \sim R e_s^{1/2}/Da$, where $Da \equiv \tau_r/\tau_k$ is the Damköhler number giving the ratio of the reaction time and the outer time scale. Thus when Da is sufficiently large, as is typically the case for most practical fuel-air combustion systems, the time required for chemical reaction is negligible in comparison with the time required for diffusion. The chemistry is then “mixing-limited”, and consequently the reaction rate is determined entirely by the mixing rate. Moreover the diffusion-to-cascade time scale ratio becomes $\tau_v/\tau_s \sim R e_s^{-1/2}$. Consequently, when Re_s is large, as is the case in practical high-speed propulsion systems, the diffusion time becomes negligible in comparison with the entrainment and cascade time. The mixing process is then “entrainment-limited”, and in that case both the mixing rate and the combustion rate are determined entirely by the entrainment rate. In practical high-speed propulsion systems, combustion occurs in turbulent shear flows under conditions that involve such mixing-limited reaction and entrainment-limited mixing. The propulsion system performance therefore depends mainly on the ability to achieve sufficiently large rates of entrainment of oxidizer into the injected fuel stream within the combustor.

1.1 Previous work

Accordingly, basic research has focused on studies of entrainment and mixing in certain fundamental supersonic turbulent shear flows, with the supersonic mixing layer being by far the most widely studied flow. Its relative simplicity and the extensive documentation of its large scale structure and dynamics under incompressible flow conditions make it well suited for this purpose. Several specific effects of compressibility have been observed from such studies. These include changes in the similarity scaling properties of the flow, in particular a reduction in the growth rate with increasing convective Mach number M_c , and an attendant reduction in the entrainment and mixing rates achieved by the flow, as well as changes in the structure and dynamics of the large scales, including a loss of two-dimensional spanwise coherence of the large scale vortical structures. Numerous studies have investigated these phenomena (*e.g.*, Bogdanoff 1982, Chinzei *et al* 1986; Papamoschou & Roshko 1988; Samimy & Elliott 1990; Elliott & Samimy 1990; Dimotakis 1991; Goebel & Dutton 1991; Papamoschou 1991,

1992; Clemens 1991; Samimy *et al* 1992; Zeman 1992; Clemens & Mungal 1992*a,b*, 1995; Gruber *et al* 1993; Hall *et al* 1993; Barre *et al* 1994; Elliot *et al* 1995). Recent studies using planar PIV measurements have revealed additional details of these phenomena (*e.g.*, Urban & Mungal 1997; Urban *et al* 1998; Olsen & Dutton 1999). While most studies correlate the observed reduction of the growth rate with increasing convective Mach number M_c , this parameter was derived by matching stagnation pressures (Bogdanoff 1982) and its applicability in the presence of “eddy shocklets” (*e.g.*, Papamoschou 1991; Hall *et al* 1993; McIntyre & Settles 1991) has been questioned. The existence of such shocklets remains unresolved, although direct numerical simulations by Lee *et al* (1991) and Umemura *et al* (1996) show the possible presence of such eddy shocks.

Among other fundamental turbulent shear flows, turbulent wakes are also known to have a strongly pronounced and comparatively well-organized large-scale vortical structure, having alternating signs of circulation. The origin of these structures has been subjected to stability analyses (*e.g.*, Papageorgiou & Smith 1989; Noack & Eckelmann 1994), and the resulting entrainment and mixing properties in incompressible planar turbulent wakes follow classical power-law scalings that are by now reasonably well understood (*e.g.*, Wygnanski *et al* 1986; Cimbala & Roshko 1988). In contrast to such incompressible wakes, supersonic wakes are formed by a body in a supersonic free stream. These can be grouped into two categories, depending on the type of wake generator. The first, termed “slender-body wakes”, are formed by a body (often an airfoil or splitter plate with a sharp trailing edge) that is significantly thinner than its boundary layer thickness. The second, termed “bluff-body wakes”, are formed when the trailing-edge thickness is much larger than the boundary layer thickness, so that the boundary layer separates from the wake generator.

Several studies have been conducted of the supersonic slender-body wake, which is characterized by weak shock and expansion waves at the trailing edge of the splitter plate. Bonnet *et al* (1984) investigated the supersonic slender-body wake created by merging turbulent boundary layers, and from hot-wire anemometry found that space

and space-time correlation features of the far-field wake did not match those in the incompressible wakes. Subsequently, Bonnet & Chaput (1986) investigated structural features by visualizing the flow using acetone seeding, and showed that no detectable large scale structure existed in the near field, whereas distinctive large scale structures were present in the far field. Chen *et al* (1990) investigated the stability of supersonic slender-body wakes by direct numerical simulation (DNS) and found a 40% reduction in the temporal amplification rate compared to the corresponding incompressible wake. Clemens & Smith (1996) presented results for transition and the development of large scale structures in a supersonic slender-body wake created by merging laminar boundary layers on a splitter plate. They found similar large scale structures as seen in incompressible wakes, and shocklets stemming from vortical structures at downstream locations where an appropriately defined relative Mach number was sufficiently high.

In contrast to supersonic slender-body wakes, supersonic bluff-body wakes create strong expansion and recompression waves in a relatively complicated base flow region. Most early studies of supersonic bluff-body wakes focused on flow properties in the base flow region (*e.g.*, Lees 1964; Lykoudis 1966; Berger 1971). More recent work on the base flow region has used optical methods to measure the velocity field, including Herrin & Dutton (1994) who measured the mean velocity and turbulence fields using LDV, and Lachney & Clemens (1998) who reported results from PLIF measurements of pressure and temperature. Sato *et al* (1999) have investigated mixing control in supersonic bluff-body wakes via forcing introduced by the mass injection rate from the bluff body into the wake. They used a wall-mounted cavity which induced an acoustic disturbance, and found an enhanced growth rate in the wake. Umemura & Takihana (1997, 1998) investigated a slot-injected planar supersonic near-field wake by DNS stability analysis, and found that Mach wave interactions due to a reflected expansion wave enhance the instabilities of the wake and the associated feedback mechanism.

To date, however, there have been few detailed studies of the supersonic planar turbulent bluff-body wake that span from the base flow region well into the self-

similar far-field wake. Only Amatucci *et al* (1992) have documented the entire velocity field by two-component LDV measurements, showing profiles of mean velocity and turbulence statistics in the near- and far-fields of a supersonic bluff-body wake. No studies to date of the supersonic bluff-body turbulent wake have involved analyses of data in terms of the scaling properties of the wake, and no detailed comparisons have been made with corresponding incompressible turbulent wakes to determine the effects of compressibility on the entrainment and mixing processes in a manner analogous to that done in supersonic turbulent mixing layers.

1.2 *Present study*

As noted above, studies of supersonic turbulent mixing layers have identified several specific effects of compressibility on the large scale structure and associated scaling properties of that flow. Since previous investigations of other supersonic turbulent shear flows have provided only limited documentation of compressibility effects on the fundamental scaling properties and large scale structure of those flows, it is widely believed that many of the compressibility effects seen in supersonic turbulent mixing layers are generic to all turbulent shear flows, and would be seen in an analogous form in other flows under locally supersonic conditions. Yet it appears likely that at least some of the compressibility effects seen in mixing layers are due to the particular large scale structure and dynamics of that turbulent shear flow, and that other fundamental turbulent shear flows with other large scale structure and scaling properties may show some of the compressibility effects seen in mixing layers, but may also demonstrate certain other phenomena not seen in mixing layers.

With this motivation, the present study was undertaken as an experimental investigation of supersonic, planar, turbulent, bluff-body wakes, to help clarify the generic effects of compressibility on entrainment and mixing in supersonic turbulent shear flows. Figure 1 shows the notation used throughout this study to describe various aspects of the wake. The emphasis is on experimental observations and detailed comparisons with corresponding results from incompressible wakes to identify effects of compressibility in the supersonic, turbulent, bluff-body wake.

The study provides results from planar laser Mie scattering (PLMS) visualizations of the vortical structure and growth of a supersonic, planar, turbulent, bluff-body wake at Mach 2 and Mach 3 conditions, together with pressure measurements to determine mean velocity fields and scaling properties of these wakes. Interpretation of the results is supported by conventional schlieren and shadowgraph imaging of the wave structure of the flow. The results and discussion presented here augment and expand initial results of Nakagawa & Dahm (1999, 2000).

This FinalReport is organized as follows. The experimental facility and the diagnostic techniques used are described in §2. Results from flow visualizations and pressure measurements are used to obtain similarity profiles, relative Mach number profiles, the flow width scaling, and the centerline velocity defect scaling in §3. Observed effects of expansion wave interactions with the large scale structure of the wake are discussed in §4, and a summary of the major conclusions drawn from this investigation is presented in §5. The Appendix provides certain peripheral results and additional background information necessary to understand and interpret the main results presented here.

2. Experimental facility and diagnostics

This section describes the experimental techniques used in this study, including description of the flow facility (§2.1), the shadowgraph and schlieren imaging system (§2.2), the planar laser Mie scattering (PLMS) imaging system (§2.3) used for flow visualization, and the pressure measurements used to obtain mean velocity fields (§2.4).

2.1 *Flow facility and test section*

The experiments were conducted in the Michigan Supersonic Mixing and Combustion Facility, shown in figure 2, which was specifically designed for studies of supersonic coflowing turbulent jets and wakes. Primary components and capabilities include a test section with stagnation temperature up to 600 K and nominal stagnation pressure of 653 kPa, a 250 kW electric air heater capable of

heating air flows up to 1.0 kg/s to temperatures as high as 1100 K, with a digital control circuit maintaining constant stagnation temperature to within ± 0.5 K in the settling section, a gas sampling system, and a suite of advanced laser diagnostics.

Figure 3 shows the test section, which has interior cross-sectional dimensions of 34.6 mm \times 38.4 mm and is 553 mm in length. There are 8 probe ports on each of the test section sidewalls, which allow pressure probe measurements along the transverse direction at several streamwise locations. Except where noted otherwise, the test section sidewalls were kept parallel for all results presented here. Any variations in wall static pressure due to the displacement effect of the wake flow itself were negligible in comparison with variations induced by the repeated reflections of the wake expansion and recompression waves from the tunnel side walls. The test section has a 38.5 mm \times 229 mm Vycor window on each of the front and back walls. Two side windows each have a 7.5 mm \times 229 mm viewing area and replace the pressure-port side walls to allow access for optical diagnostics.

As indicated in figure 3, the test section was outfitted with a subsonic slot nozzle centered in the test section entrance plane, having exterior dimensions of 4.2 mm \times 38.4 mm and interior dimensions of 2.0 mm \times 36.2 mm. This slot nozzle entered the tunnel through a 1/4-in. ID round tube, and then flattened in the spanwise direction as it extended into the test section 2 mm past the end of the supersonic nozzle. The slot nozzle was packed with glass beads and screens to produce a uniform low-speed flow across the exit plane of the slot, typically in the range of 50 - 100 m/s, corresponding to volume flow rates typically below 1.0×10^{-3} m³/s. The Reynolds numbers Re_L based on the length L from the throat of the supersonic nozzle to the end of the slot nozzle were sufficiently large (see table 1) that the boundary layers on the outside of the slot nozzle wall were turbulent. These boundary layers produced a drag per unit span $D = \rho_\infty U_\infty^2 \vartheta_{BL}$ that greatly exceeded the momentum per unit span $J_0 = \rho_0 U_0^2 b_0$ introduced by the flow through the slot nozzle, where ϑ_{BL} is the boundary layer momentum thickness, and b_0 denotes the width of the slot nozzle. The nozzle thus acted as a bluff-body wake generator, with the flow through it serving mainly to permit visualization of the resulting turbulent

wake. The resulting net drag

$$(D - J_0) \equiv \rho_\infty U_\infty^2 \vartheta, \quad (1)$$

produced a wake momentum thickness ϑ (see Appendix) which, in the absence of any pressure gradient, is essentially constant at all downstream locations in the wake.

The supersonic nozzles were designed with the inviscid NOZCS3 program to produce wave-free Mach 2.0 and Mach 3.0 free stream flows, taking into account the presence of the slot nozzle. However, owing to the relatively small cross section of the test section, the boundary layers along the supersonic nozzle and sidewalls, and along the outer walls of the slot nozzles, produced a significant reduction in the effective cross sectional area of the tunnel. In addition, estimated total pressure losses for the Mach 2 and Mach 3 cases were about 5% and 20% respectively, and were attributed to imperfections in the nozzle. For the higher Mach number, the larger total pressure loss is due to the longer nozzle length. These factors combined to lower the two free stream Mach numbers entering the test section (on either side of the slot nozzle) from the original design values to 1.86 and 1.73 for the Mach 2 wake, and to 2.66 and 2.57 for the Mach 3 wake, as indicated in table 1.

2.2 *Shadowgraph and schlieren imaging*

A long path length shadowgraph and schlieren imaging system was used to document the wave patterns in the near-field expansion and recompression region and throughout the test section for both the Mach 2 and Mach 3 cases. Light from a Xenon Corp. Nanolamp with 20 ns pulse duration passed through focusing optics consisting of a microscope objective ($16 \times$), a pinhole ($\phi = 400 \mu\text{m}$), and a spherical lens ($f = 100 \text{ mm}$). Two parabolic mirrors (205 mm OD, $f = 1890 \text{ mm}$) and two flat mirrors (240 mm and 50 mm OD) were used. The light was imaged directly onto a thermoelectrically cooled 512×512 CCD array (Princeton Instruments, Inc.) with 1 ms minimum shutter speed. The time resolution of the system was thus set by the 20 ns light pulse duration. The camera controller (Princeton Instruments ST138S) triggered the nanolamp through a delay generator (Berkeley Nucleonics Corp.

Model 7010). Images were captured through a PCI board using image acquisition software (Princeton Instruments WinView 32) on a PC computer. The 8 m long optical path length, measured from the test section to the CCD camera, provided good sensitivity of the system. All system components were mounted on a milling machine base and lab jacks to permit stable height adjustments that allowed imaging over the entire wake region of interest.

2.3 Planar Laser Mie Scattering (PLMS) Imaging

Since shadowgraph and schlieren imaging integrates the flow structure across the test section, a planar laser Mie scattering (PLMS) imaging system was used to document the instantaneous two-dimensional structure and the visual width $\delta(x)$ of the wake. The PLMS technique (Clemens & Mungal 1991) uses alcohol vapor seeded in the free stream of a supersonic mixing layer to visualize the flow. Clemens (1991) describes this PLMS technique in detail, including Mie scattering theory, particle sizing of alcohol vapor, and its thermodynamic properties (*e.g.*, vaporization, condensation, and coagulation). Although the Mie-scattered signal does not represent a conserved scalar, it nevertheless is capable of revealing the instantaneous structure of the mixing region. Ensemble-averaged images of the PLMS intensity across the flow allow the visual width to be determined.

In the present experiment, ethanol vapor was introduced in the air issuing from the slot nozzle by spraying liquid ethanol into a seeder, approximately 1 m upstream of the nozzle exit. The seeder was heated to a temperature around 50 °C by a band heater to promote rapid vaporization. Ethanol vaporized in the air stream before exiting the nozzle, with the resulting mass fraction of alcohol typically below 1% to avoid formation of large droplets which would not follow the fluid motion. When the ethanol vapor mixed with the cold, supersonic free stream air (see table 1) it condensed to form a fine fog. For the free stream temperature and flow conditions used here, fog droplet sizes are believed to be below 20 μm (Clemens & Mungal 1991). A 532 nm laser sheet formed from a Nd:YAG laser (Spectra-Physics Quanta-Ray Pro-Series) with 10 ns pulse duration and energy of approximately 80 mJ/pulse passed through the wake with approximately 5 mm thickness. Mie

scattering from the ethanol fog was then imaged onto the same CCD camera described in §2.2.

2.4 Pressure measurements

The sidewall static pressure distribution was monitored with a total of 16 sidewall pressure taps on the left and right sidewalls as indicated in figure 3. For each Mach number, wall static pressures were measured by pressure taps on the front and back side of the wall. Each wall consisted of three rows of pressure taps; one row was located on the test section centerline and two others located 0.4-in on either side of the centerline. Each row consisted of 15 taps. Pitot pressures were measured along the transverse direction in fine increments at 25 downstream locations in the Mach 2 wake, and at 16 downstream locations in the Mach 3 wake, using 0.025-in pitot probes. Five such probes with different lengths were made to allow pitot pressure measurements at virtually any streamwise location. The probes were designed following established principles for supersonic flows (Pope & Goin 1965). The probe position was adjusted manually along the transverse direction using a digital micrometer (Mitutoyo Corp. Digimatic). Pressure was monitored with a pressure gauge (Ashcroft; 0.5 in. Hg subdivision for vacuum; 0.2 psi subdivision; Accuracy: Grade 3A 0.25%). The measured pitot pressure profiles were converted to Mach number profiles at each downstream location using the Rayleigh supersonic pitot formula, and subsequently converted to velocity profiles using the adiabatic flow relation as described in §3.2. Nominal experimental conditions based on these pressure measurements are summarized in table 1.

Ideally, static pressure profiles would have been measured at the same transverse positions where the pitot pressures were measured. However due to clearance problems between the probe and the slot nozzle in the near-field, static pressures could be measured only on the test section centerline. Consequently, any static pressure variations along the transverse direction were not taken into account. As in most free shear flows, static pressure variations in the wake far field are expected to be small, however in the near field there may be significant variations near the edges of the wake where the static pressure transitions from the value inside the

recirculation zone to that in the free stream. Since these velocity profiles were used to measure the wake velocity width $\delta_{1/2}(x)$, any error introduced by this approximation could affect the near-field results.

3. Experimental results

As noted in §1 and in the Appendix, the mixing rate is entrainment-limited and the entrainment rate is, in turn, set by the growth rate of the local outer scale $\delta(x)$ associated with the mean flow in the wake. Accordingly, §3.1 presents results from PLMS and shadowgraph visualizations of the mixing properties and wave structure of the wake. Following this, §3.2 provides results of pressure measurements from which mean velocity profiles are obtained, and in §3.3 these are used to determine the relative Mach number $M_r(x)$, the scaling properties associated with the visual and velocity widths $\delta(x)$ and the mean centerline velocity deficit $u_0(x)$. The effects of periodic forcing produced by interactions between reflected expansion waves and the wake on the power-law scalings of $\delta(x)$ and $u_0(x)$, and thus on the scaling constants that determine the entrainment and mixing rate, are examined in §3.4.

3.1 PLMS and shadowgraph visualization results

3.1.1 Base flow region

Figure 4 gives a schematic representation of the major features associated with classical two-dimensional supersonic base flows with mass injection, including the present supersonic bluff-body wake. Such wave patterns in the base flow region of supersonic wakes have been documented by many studies (*e.g.*, Alber & Lees 1968; Berger 1971, Amatucci *et al* 1992; Herrin & Dutton 1994). The free shear layers resulting from the separated boundary layers on the top and bottom surfaces of the bluff body are turned by an expansion fan through the angle required to match the base pressure in the recirculation region (see §A.3.2). The separated shear layers merge near the centerline, where the turning required by symmetry to realign the flow in the streamwise direction produces compression waves. The compression waves merge into a wake recompression shock, which subsequently interacts with the expansion fan. In an unconfined flow, these waves produce no further effect on

the turbulent wake that forms beyond the resulting “neck”. However in a confined flow, such as the present facility or in a practical scramjet combustor, these waves are reflected and intersect the wake flow further downstream.

These features can be seen in the shadowgraph visualizations shown in figure 5, where results are given for various mass flow rates through the slot nozzle in the Mach 2 wake. When there is no mass flow through the nozzle (*i.e.*, figure 5*a*), the expansion and recompression process in the base flow region is seen to occur within a relatively short distance past the nozzle exit, and the extent of the base flow region is set by the slot width. In the remaining images, corresponding to increasing mass flow rates through the slot nozzle, the base flow region becomes much longer and the compression wave is seen to broaden considerably. Moreover, with increasing injection rate, the wake shock is seen to become weaker and the expansion wave presumably also weakens, since the volume displaced by the inflow requires the free stream to be turned through a smaller angle.

Furthermore, with increasing injection pressure the stagnation streamline and the dividing streamline in the base flow separate to accommodate the injected mass flow rate. The resulting displacement effect reduces the angle through which the expansion fan must turn the flow, and thereby causes the base flow region to extend further downstream, as is evident in figure 5. Through this mechanism, it is anticipated that the mass injection rate will affect the virtual origin x_0 of the resulting far-field wake flow (see §A.3). The conditions used throughout the remainder of this investigation involved exceedingly low injection rates, and thus correspond most closely to figure 5*a*.

3.1.2 Near-field region

Instantaneous shadowgraph and PLMS images of the base flow and near-wake region for the Mach 2 case are shown in figures 6 and 7, respectively. The PLMS images correspond to a small mass injection rate at the wake generator, and show the major features of the base flow region indicated in figure 4. In the PLMS images in figure 7, there are no quasi-periodic, large scale, organized structures

apparent over the imaged region of the flow, though this will be examined in greater detail in later sections. Also, no evidence of “eddy shocklets” of the type seen in previous studies by Clemens & Smith (1996) in slender body wakes, was found in these PLMS and shadowgraph images of the bluff-body wake.

3.1.3 *Far-field region*

Instantaneous PLMS images

Figures 8 and 9 show three typical examples of the resulting instantaneous PLMS images for the Mach 2 and Mach 3 wakes, respectively, spanning from the nozzle exit well into the wake far field. The comparatively steady base flow region can be seen at the extreme left side of these images for the Mach 2 wake in figure 8. At about $x = 3$ cm downstream of the slot nozzle, large-scale organized vortical structures with alternating signs of circulation can be seen to begin forming. By about $x = 6$ cm, these structures typically have organized into a characteristic, quasi-periodic, vortex street-like pattern that continues downstream. The wake can be seen to broaden slowly with increasing downstream distance. The size and spacing of the vortical structures appear to increase with the wake width.

Unlike the Mach 2 wake in figure 8, in the Mach 3 case in figure 9 the Mie scattering intensity seen in these PLMS images was very weak up to about $x = 4$ cm. To understand this, note that condensation of the ethanol vapor introduced by injection at the wake generator does not occur until the injected fluid mixes with the much colder supersonic free stream fluid. Clemens (1991) notes that the volume fraction of cold free stream fluid in ethanol-containing fluid must be at least 20% for the ethanol vapor to begin condensing. This would suggest that, upstream of $x = 4$ cm in figure 9, the mixing between the slot-jet fluid and the free stream fluid may not have reached this value, while in the Mach 2 wake in figure 8 sufficient mixing occurs almost immediately beyond the slot-jet exit for condensation to occur. Since the relative Mach number $M_r(x)$, defined as the Mach number difference between the wake centerline and the free stream flow [see (5)], is highest at these relatively early locations in the Mach 3 wake, this might suggest a reduction in mixing in the

supersonic wake with increasing relative Mach number. It will be seen elsewhere in the present study that this is in fact the case.

Equally important, at about 4 cm downstream of the slot nozzle in the Mach 3 wake in figure 9, a distinct “zig-zag” pattern begins to appear that is presumably indicative of the development of large-scale organized structures. However, the transition from this initial formation process around $x = 4$ cm to the much larger vortical structures evident over the range from 7 cm to 12 cm is far more dramatic than the large-structure evolution seen in the Mach 2 wake in figure 8. Indeed, the large-scale structures seen over this range in figure 9 have a fundamentally different appearance than do the structures in the Mach 2 wake in figure 8. Also, over this same range of downstream distance x , the Mach 3 wake grows at a much faster rate than does the Mach 2 wake. At the same time, figure 9 suggests that this increase in the wake width appears to result principally from increased entrainment of free stream fluid into the wake, rather than from increased mixing between free stream fluid and wake fluid. Moreover, at even larger downstream distances x in figure 9, the Mach 3 wake appears to show a reduction in width with further increase in downstream distance x , instead of the continued growth that might normally be expected. Additional evidence relevant to the origin of this phenomenon will be presented below, and the precise mechanism responsible for these phenomena will be discussed in §4.4.

Ensemble-averaged PLMS images

Figures 10 and 11 show ensemble-averages of 80 instantaneous PLMS images of the type in figures 8 and 9, respectively, together with typical instantaneous shadowgraph images on which the mean PLMS images are superimposed. The growth in the visual thickness of the wake with increasing downstream distance can be clearly seen, as can the slight deflections of the wake by small asymmetries in the reflected expansion and compression wave patterns. The asymmetries result from slight mismatches in the free stream Mach numbers entering the test section on either side of the slot-jet nozzle, as seen in table 2, due to small imperfections in centering the nozzle within the test section.

Note that, at the higher Mach number, the angles of the expansion and recompression waves become shallower, and consequently the reflected waves intersect further downstream than in the Mach 2 wake. The darker regions in the PLMS images near $x/\theta = 180$ and 330 in figure 10 for the Mach 2 wake, and near $x/\theta = 200$ in figure 11 for the Mach 3 wake, can be seen to coincide with interactions between the wake flow and the reflected recompression shock. The wake shock intersection can also be seen in the mean PLMS image for the higher Mach number wake in figure 11. The same figure also shows the dramatic increase in the growth rate of the wake, beginning near $x/\theta \approx 120$, that was suggested by the zig-zag structure in figure 9. Beyond the downstream location where the shock wave intersections with the wake occur in figure 11, the mean PLMS image also shows the reduction in visual width of the wake as noted in figure 9.

Lateral profiles of the mean PLMS intensity at several downstream locations in the Mach 2 and Mach 3 wakes are shown in figure 12. The small deflections of the wake centerline noted above, indicated here by the peaks in these profiles, are readily apparent in both cases. To quantify the visual thickness of the wakes, a Gaussian fit was determined for each PLMS profile by computing the three lowest moments over the central portion of the flow and matching these to a Gaussian function. This allowed the local centerline position $y_0(x)$, the local maximum PLMS intensity, and the local visual width $\delta_{1/2}(x)$ of each profile to be determined. Here $\delta_{1/2}(x)$ denotes the half-width at the half-maximum point of the local intensity profile. The resulting $\delta_{1/2}(x)$ for each wake are of particular interest, since these determine the entrainment and mixing rate of the wake flow as noted in the Appendix. The values obtained will be discussed in §3.3, together with analogous widths obtained from measured pitot pressure profiles in the following section.

3.2 Pressure measurement results

3.2.1 Pressure profiles

Pitot pressure profiles were measured for the Mach 2 and Mach 3 wakes to obtain

the width $\delta_{1/2}(x)$ of the mean velocity profiles for each case. The pressure was measured in 0.5 mm increments along the transverse direction at 21 downstream locations in the Mach 2 wake, and in 0.25 mm increments along the transverse direction at 16 downstream locations in the Mach 3 wake. Figure 13 shows the resulting pitot pressure profiles at the first eight downstream locations in the Mach 2 wake, superimposed on a shadowgraph image to allow the wave structure of the flow to be reconciled with these profiles. This shows the extent of the expansion fan and the point where the trailing wave in the expansion fan intersects the wake shock.

The wall static pressures, measured along the downstream direction on the centerline of the test section and at 0.4-in on either side of the centerline, are shown in figure 14a for the Mach 2 wake and in figure 14b for the Mach 3 wake. These pressure variations are consistent with the pattern of repeated expansion and compression wave reflections seen in figures 10 and 11. Taking static pressure variations across the wake to be small, the pitot pressure profiles were converted to local Mach number profiles $M(y)$ by the Rayleigh supersonic pitot formula

$$\frac{p}{p_{02}} = \frac{\left(\frac{2\gamma}{\gamma+1} M^2 - \frac{\gamma-1}{\gamma+1} \right)^{1/(\gamma-1)}}{\left(\frac{\gamma+1}{2} M^2 \right)^{\gamma/(\gamma-1)}}. \quad (2)$$

Here γ is the specific heat ratio, p is the static pressure, for which the centerline value was used, and p_{02} is the measured pitot pressure (*i.e.*, the total pressure behind the normal shock produced by the pitot probe). The resulting Mach number profiles were then converted to mean velocity profiles $U(y)$ assuming adiabatic flow as

$$\frac{U}{a_0} = \sqrt{\frac{2}{(2/M^2) + (\gamma-1)}}, \quad (3)$$

where a_0 is the acoustic speed at stagnation conditions given by $a_0 = \sqrt{\gamma RT_0}$. The resulting $U(y)$ profiles were then converted to mean velocity defect profiles $u(y) \equiv U_\infty(x) - U(y)$. Together with the local free stream Mach number $M_\infty(x)$ obtained as described in the following section, these velocity defect profiles were then used to

determine the local relative Mach number $M_r(x)$ in §3.2.4 and the resulting scaling properties of the flow width $\delta_{1/2}(x)$ in §3.3.1 and the peak defect velocity $u_0(x)$ in §3.3.2.

3.2.2 Freestream Mach number $M_\infty(x)$

From the free stream static pressure measurements in figures 14a,b, local values of the free stream Mach number $M_\infty(x)$ were obtained via (2) for the Mach 2 and Mach 3 wakes, as shown in figure 15a,b. Note that unlike the supersonic mixing layer or the supersonic slender-body wake, which do not produce strong waves, the supersonic bluff-body wake inherently produces strong expansion and recompression waves, as seen in figures 6, 10, and 11. Reflections of these waves from the side walls thus lead to Mach number variations as well as density variations in the free stream, and consequently a single “free stream Mach number M_∞ ” cannot be defined.

For the Mach 2 wake, the Mach number $M_\infty(x)$ entering the test section (*i.e.*, at $x = 0$) on either side of the slot-jet was 1.86 and 1.73, as noted in table 2. As seen in figure 15a, the free streams are accelerated to $M_\infty(x) \approx 2$ by the expansion wave created at the corner of the slot nozzle, and then decreased to $M_\infty(x) \approx 1.7$ after passing through the wake shock. Thereafter $M_\infty(x)$ gradually increases again up to about 1.8 as it passes through the reflected expansion wave, until reaching the reflected shock wave around $x/\theta = 120$. For the Mach 3 wake in figure 15b, the free stream Mach numbers $M_\infty(x)$ entering the test section were 2.66 and 2.57 (see table 2), with subsequent variations created as the free streams passed through the pattern of expansion and shock waves.

3.2.3 Similarity profiles

The mean velocity defect profiles $u(y)$ obtained in §3.2.1 were fitted with a Gaussian profile in the same manner as the mean PLMS profiles in §3.1.3 to determine the local centerline location $y_0(x)$, the local centerline velocity defect $u_0(x)$, and the local flow width $\delta_{1/2}(x)$ of each profile. The resulting values of the local outer variables $\delta_{1/2}(x)$ and $u_0(x)$ allowed each profile to be scaled to assess the

self-similarity of the flow. Thus the measured velocity defect profiles $u(y)$ were each normalized by their local centerline velocity defect $u_0(x)$, with y centered on $y_0(x)$ and normalized by $\delta_{1/2}(x)$.

The results are shown in figures 16a,b for the Mach 2 and Mach 3 wakes, respectively. It is apparent that all of the profiles shown are very nearly self-similar for the Mach 2 wake in figure 16a. The same holds for the Mach 3 wake in figure 16b except at the first two locations shown, where near-field effects lead to departures from self-similarity. The results in figure 16 thus indicate that compressibility effects in supersonic wakes do not invalidate the fundamental self-similarity traditionally associated with incompressible turbulent shear flows, despite the complex wave interactions noted above. Furthermore, this demonstrates that any effects of compressibility on the mean flow properties are embodied entirely in the local outer variable scalings $\delta_{1/2}(x)$ and $u_0(x)$. Accordingly, the main emphasis in the remaining results is on determining the effects of compressibility on these outer variable scalings.

It well known that the scaling laws for $\delta_{1/2}(x)$ and $u_0(x)$ in incompressible, planar, turbulent wakes are properly expressed in terms of the momentum thickness ϑ , given by

$$\vartheta = \frac{D - J_0}{\rho_\infty U_\infty^2} = \int_{-\infty}^{+\infty} \frac{U(y)}{U_\infty} \left(1 - \frac{U(y)}{U_\infty} \right) dy, \quad (4)$$

which is invariant with downstream location x in incompressible wakes. In view of the self-similarity of the mean velocity profiles demonstrated in figures 16a,b, it is apparent that the invariance of the momentum thickness in (4) is determined by the scalings for $\delta_{1/2}(x)$ and $u_0(x)$. The local momentum thickness $\vartheta(x)$ determined by integrating each of these velocity defect profiles as indicated in (4) was found to be essentially invariant with downstream distance x up to the point where the expansion waves interact with the wake, yielding $\vartheta(x) = 0.40 \pm 0.03$ mm for the Mach 2 wake and 0.55 ± 0.07 mm for the Mach 3 wake.

3.2.4 Relative Mach number $M_r(x)$

The relative Mach number $M_r(x)$, defined in terms of the mean centerline velocity defect $u_0(x) \equiv U_\infty - U_0(x)$ and the free stream acoustic speed, serves a corresponding role in the supersonic wake as an indicator of the relative importance of compressibility as does the convective Mach number M_c in the supersonic mixing layer. Thus

$$M_r(x) = \frac{u_0(x)}{a_\infty}. \quad (5)$$

where $a_\infty = \sqrt{\gamma R T_\infty}$, and

$$\frac{T_0}{T_\infty} = 1 + \frac{\gamma - 1}{2} M_\infty^2, \quad (6)$$

with a_∞ and T_∞ giving the acoustic speed and temperature, respectively, in the free stream. Unlike the mixing layer, for which M_c does not vary with downstream location x , in the wake the velocity defect $u_0(x)$ must decrease with increasing x , and thus the relative Mach number $M_r(x)$ must also decrease with x . As a consequence, supersonic turbulent wakes will naturally evolve from comparatively large compressibility effects at relatively small values of the downstream location x , where the local relative Mach number $M_r(x)$ may be quite large, to an essentially incompressible wake flow at downstream locations sufficiently large for the local $M_r(x)$ to have decreased to near-zero values.

Figures 17a,b show the resulting relative Mach number $M_r(x)$ at each location x , from the measured centerline velocity defects $u_0(x)$ in figures 16a,b and the free stream Mach numbers $M_\infty(x)$ in figures 15a,b. It is apparent that, in both cases, $M_r(x)$ decreases rapidly, and that the wake is at nearly incompressible local flow conditions over most of the range of downstream locations shown in figures 8 - 11. However, in supersonic turbulent mixing layers, reductions in the layer growth rate $d\delta/dx$ of at least 20% relative to the incompressible mixing layer are observed even at convective Mach numbers as low as 0.2. This suggests that, if observations in supersonic mixing layers are indeed indicative of generic effects of compressibility in other turbulent shear flows, then figures 17a,b would imply that clearly

measurable compressibility effects should be expected up to at least $(x/\vartheta) \approx 100$ for the Mach 2 case, and up to $(x/\vartheta) \approx 150$ for the Mach 3 case, for which $M_r(x)$ exceeds 0.2.

In the following sections, observed effects of compressibility in the present Mach 2 and Mach 3 supersonic turbulent wakes will be correlated with the corresponding local values of the relative Mach number $M_r(x)$.

3.3 Scaling properties: incompressible wake comparisons

To look for effects of compressibility in the supersonic wake analogous to those observed in supersonic mixing layers, we compare the local outer variable scalings $\delta_{1/2}(x)$ and $u_0(x)$ to corresponding results from incompressible, planar, turbulent wakes. These outer variable scalings determine the local entrainment rate into the wake. In incompressible planar turbulent wakes, the outer variable scalings in the self-similar far field have been relatively well established. In particular, the flow width scales with the wake momentum thickness as

$$\frac{\delta_{1/2}(x)}{\vartheta} = c_\delta \left(\frac{x - x_0}{\vartheta} \right)^{\frac{1}{2}}, \quad (7)$$

and the centerline velocity defect as

$$\frac{u_0(x)}{U_\infty} = c_u \left(\frac{x - x_0}{\vartheta} \right)^{-\frac{1}{2}}. \quad (8)$$

The scaling constants c_δ and c_u , and the virtual origin x_0 , depend on the wake generator. For bluff-body wakes, Wynanski *et al* (1986) find

$$c_\delta = 0.270, \quad (9)$$

$$c_u = 1.88, \quad (10)$$

and

$$\left(\frac{x_0}{\vartheta} \right) = -128. \quad (11)$$

For later reference, various other steady wake generators give $c_\delta = 0.29 \pm 0.03$ and $c_u = 1.70 \pm 0.2$ (Wynanski *et al* 1986). These constants are summarized in table 2. It is of interest to compare these power-law scalings and the constants for

incompressible wakes with the present results from supersonic wakes.

3.3.1 Flow width scaling $\delta(x)$

In view of the incompressible flow width scalings in (3.9), figures 18a and 19a show $(\delta_{1/2}/\vartheta)^2$ plotted against (x/ϑ) for the Mach 2 and Mach 3 wakes, respectively. The circles denote the visual width $\delta_{1/2}(x)$ determined from moments of the lateral mean PLMS intensity profiles in figures 12a,b (see §3.1.3). The squares denote $\delta_{1/2}(x)$ determined from moments of the mean velocity defect profiles $u_0(x)$ in figures 16a,b. If the present supersonic wakes follow the same 1/2-power-law scalings as do their incompressible counterpart, then the symbols in figures 18a and 19a should fall on straight lines, with the slopes being related to the scaling constant c_δ , and the virtual origin (x_0/ϑ) being identifiable by the x-intercept. The results for the Mach 2 and the Mach 3 wakes are discussed separately in the following sections.

Mach 2 wake

Consider first the circles in figure 18a, which give the visual width $\delta_{1/2}(x)$ determined from the first three moments of lateral mean profiles of the PLMS intensity in the Mach 2 wake, such as those shown in figure 12a. The first few points are within the base flow region in the near field and, as would be expected from figure 6, these show $\delta_{1/2}(x)$ decreasing with increasing x due to the narrowing effect of the expansion and recompression process. Beyond the recompression zone, the wake widths $\delta_{1/2}(x)$ for the next fifteen points increase in accordance with the 1/2-power-law scaling noted above, as is evident from the straight line fit to these points.

The virtual origin implied by the intercept of this straight line fit gives

$$\left(\frac{x_0}{\vartheta} \right)_{\text{vis}} = -31, \quad (12)$$

for the compressible wake. This downstream shift of the virtual origin relative to the incompressible value of -128 in (11) is not unexpected (see §§A.2 and A.3), given the reduction in wake width created by the expansion and recompression process in the base flow region (see §3.1.2). The value in (12) pertains to the

relatively low mass injection rate that was used to seed the ethanol vapor into the wake through the slot jet nozzle. As figure 5 suggests, this virtual origin would be expected to shift upstream (*i.e.*, become more negative) with increasing mass injection rate. At sufficiently high injection rates, (x_0/ϑ) may approach the incompressible value in (11).

The slope of the straight line fit to the circles in figure 18a implies a value of

$$c_\delta = 0.39. \quad (13)$$

for the scaling constant in the flow width scaling of the Mach 2 wake. This is remarkable in that it is higher than the value in the incompressible wake in (9), whereas experience from supersonic mixing layers would indicate a reduction in the value of the flow width scaling constant due to compressibility. While this scaling constant c_δ in the Mach 2 wake is significantly higher than the value found for any steady wake generator by Wygnanski *et al* (1986), they found that periodic forcing introduced at the wake generator can dramatically increase the scaling constant over the value obtained from the same generator without forcing (see their table 2). For such forced wakes they typically found values in the range of

$$c_\delta = 0.35 \pm 0.03, \quad (14)$$

depending on the details of the forcing, which appear to be in accord with the present value in (13). Indeed it will be seen later in this section that there is strong evidence that confined supersonic wakes experience wave-induced periodic forcing due to intersections of the reflected expansion waves with the organized vortical structures of the flow. The remainder of the circles in figure 18a, which depart from the straight line for the 1/2-power-law scaling, are related to effects of such forcing and thus will be discussed below.

The square symbols in figure 18a give the velocity width $\delta_{1/2}(x)$ obtained from moments of the mean velocity profiles in figure 16a. The first ten of these points also demonstrate a 1/2-power-law scaling, as indicated by the straight line fit through them. This gives the same value for the scaling constant as in (13), namely $c_\delta = 0.39$. Only the virtual origin is different in this case, giving

$$\left(\frac{x_0}{\vartheta} \right) = 22. \quad (15)$$

As noted in §3.1.2 and in the Appendix, the downstream shift of the virtual origin relative to the incompressible value in (11) is expected. Moreover, the fact that the virtual origin for the visual thickness in (12) is more negative than that for the velocity width in (15) appears consistent with the common observation that the scalar (visual) width of turbulent shear flows tends to be somewhat larger than the velocity profile width.

Note, however, that for $(x/\vartheta) \geq 90$ the visual width given by the circles in figure 18a no longer appears to follow the 1/2-power-law scaling of the incompressible wake. Yet these relatively far downstream locations are precisely where the relative Mach number $M_r(x)$ in figure 17a has decreased to nearly incompressible values, and where the power-law scaling would thus be expected to apply best. To understand the origin of these departures from the 1/2-power-law scaling, it is essential to note that the circles in figure 18a show two peaks centered roughly at $(x/\vartheta) = 190$ and 330, as indicated by the black arrows, which correspond respectively to $x = 7.6$ cm and 13.0 cm. Notably, these positions coincide with the locations in figure 10 where the reflected recompression shocks intersect the Mach 2 wake. Moreover, the leading Mach wave of the reflected expansion wave in figure 10 first intersects the wake at $(x/\vartheta) = 90$, indicated by the gray arrow in figure 18a, which corresponds to $x = 3.6$ cm. This is precisely where the circles in figure 18a begin to depart from the straight line giving the 1/2-power-law scaling. These observations combine to strongly suggest that the deviations from the 1/2-power-law scaling in figure 18a are connected with these wave interactions.

A further clue is provided in figure 18b, where these same data for the visual and velocity widths $\delta_{1/2}(x)$ are shown in log-log form, with the 1/2-power-law scalings given by the dashed and solid lines corresponding to the scaling constants c_δ found by Wygnanski *et al* (1986) in forced and unforced wakes. This suggests that the mechanism by which the reflected wave interactions cause the wake to depart from the $(\delta/\vartheta) \sim (x/\vartheta)^{1/2}$ scaling may be connected with the effects of forcing. This will

be explored further below after corresponding results from the Mach 3 wake have been discussed.

Mach 3 wake

Figure 19 presents analogous results for the Mach 3 wake as were given in figure 18 for the Mach 2 wake. In particular, figure 19a shows $(\delta_{1/2}/\vartheta)^2$ plotted against (x/ϑ) , with circles denoting the visual width $\delta_{1/2}(x)$ determined from mean PLMS intensity profiles such as those in figure 12b, and squares denoting $\delta_{1/2}(x)$ determined from the mean velocity defect profiles $u_0(x)$ in figure 16b. As before, except for the first few points in the near-field region, both profiles follow the 1/2-power-law scaling of incompressible wakes indicated by the straight lines, up to about $(x/\vartheta) \approx 120$. The virtual origins for the visual and velocity widths implied by the intercepts of these lines are

$$\left(\frac{x_0}{\vartheta}\right)_{\text{vis}} = -90, \quad (16)$$

and

$$\left(\frac{x_0}{\vartheta}\right) = 5, \quad (17)$$

which are again shifted downstream from the -128 value in (11) for incompressible wakes due to the existence of the base flow region (see Appendix). Moreover, the scaling constant implied by both straight line slopes is again the same for both the visual and velocity widths, and corresponds to

$$c_\delta = 0.26. \quad (18)$$

This is much lower than the value in (13) from the Mach 2 wake, and is comparable to c_δ in (9) found by Wygnanski *et al* (1986) in unforced incompressible wakes. Note that this lower value of c_δ is consistent with the downstream shift toward more negative values of the virtual origin (see §§A.2 and A.3).

Beyond $(x/\vartheta) \approx 120$, the data in figure 19a also depart from the straight line, despite the fact that the relative Mach number $M_r(x)$ in figure 17b has by that point decreased to nearly incompressible values. In this case, the departure shows only one peak over the range of downstream distances considered, now centered roughly

at $(x/\vartheta) \approx 190$ as indicated by the black arrow, which corresponds to $x = 10.5$ cm. Notably, this again coincides with the location in figure 11 where the reflected recompression shocks intersect the Mach 3 wake. Moreover, the point where the leading Mach wave of the reflected expansion wave in figure 11 first intersects the wake is at $(x/\vartheta) \approx 120$, indicated by the gray arrow in figure 19a, which corresponds to $x = 6.6$ cm. This again is precisely where the data in figure 19a begin to depart from the straight line indicating the 1/2-power-law scaling. Thus, as was suggested by the results from the Mach 2 wake, these further observations in the Mach 3 wake effectively demonstrate that the departures from the 1/2-power-law scalings in figures 18 and 19 are directly connected with these wave interactions. Although both the absolute and relative positions of the onset of these departures from the 1/2-power-law scalings, as well as the locations of the peak departures, differ dramatically between the Mach 2 and Mach 3 wakes, in both cases they coincide precisely to the location of intersections with the wake by the leading Mach wave in the reflected expansion wave and by the reflected recompression shock(s).

Regarding the physical mechanism by which these wave intersections with the wake cause such departures from the nominal wake scaling laws, an important additional clue is provided in figure 19b. This gives the same data as in figure 19a for the visual and velocity widths, but in log-log form with the dashed and solid lines giving the 1/2-power-law scalings for the scaling constants c_8 in forced and unforced wakes found by Wygnanski *et al* (1986). Note that, whereas the Mach 2 wake in figure 18b followed the forced scaling constant (*i.e.*, the dashed line), the Mach 3 wake in figure 19b appears to follow the unforced scaling constant (*i.e.*, the solid line).

This suggests a picture in which forcing in confined supersonic wakes is induced locally by interactions of the reflected expansion wave with large-scale vortical structures in the wake. The effect of this local forcing is to produce a rapid downstream increase in the growth rate of the wake (*e.g.*, Marasli *et al* 1992), leading to a local departure from the 1/2-power-law scaling beginning immediately downstream of the point where the expansion wave intersects the wake.

Furthermore, the ability of this locally induced forcing to also propagate upstream, and thereby affect the growth rate of the entire wake, depends on the existence of a subsonic path near the centerline of the wake. The presence of such a path depends on the centerline Mach number $M_0(x) = M_\infty(x) - M_r(x)$, where $M_\infty(x)$ and $M_r(x)$ are given, respectively, in figures 15a,b and 17a,b. In the Mach 2 wake, the centerline Mach number $M_0(x)$ is sufficiently low at the location $(x/\vartheta) \approx 90$ at which the reflected expansion wave first intersects the wake that such a subsonic upstream path extends to the wake generator. In the Mach 3 wake, however, two factors prevent such a subsonic path. First, the centerline Mach numbers $M_0(x)$ are inherently higher throughout the wake. Even more important, however, is that the downstream location at which the reflected expansion wave interacts with the wake is moved much farther downstream, where the centerline Mach number is supersonic, due to the shallower wave angles in that case. As a consequence, no subsonic upstream path exists along which the local forcing produced by the wave interaction with the wake can propagate upstream. The result is that, upstream of the expansion wave interaction, the Mach 3 wake is unforced and thus grows with the unforced scaling constant c_δ in (18), while in the Mach 2 wake the forcing propagates upstream and the wake in that case grows with the forced scaling constant c_δ in (13).

This picture of the origin and effects of forcing in confined supersonic turbulent wakes will be explored further below, after corresponding results for the scaling of the centerline velocity defect $u_0(x)$ in the Mach 2 and Mach 3 wakes have been discussed.

3.3.2 Centerline velocity defect scaling $u_0(x)$

Mach 2 wake

Based on the 1/2-power-law scalings in (8) for the mean velocity defect in incompressible turbulent wakes, figure 20a shows $(u_0/U_\infty)^2$ plotted against (x/ϑ) for the Mach 2 wake, where the centerline defect velocities are from §3.2.1. If the supersonic wake follows a similar power-law scaling as does the incompressible

wake, then the symbols in this figure should fall on a straight line, with the slope determining the scaling constant c_u and with the virtual origin (x_0/ϑ) identified by the x-intercept. Note that, as shown in §A.1, the scaling constant c_u considered here and the constant c_δ in §3.3.1 are related via the momentum conservation requirement.

In general, the centerline velocity defect scaling $u_0(x)$ in figure 20a shows very similar features as did the flow width scalings $\delta_{1/2}(x)$ in §3.3.1. Over roughly the same downstream region where $\delta_{1/2}(x)$ in figures 18a followed the incompressible 1/2-power-law scaling, it is apparent that the centerline velocity defect $u_0(x)$ in figure 20a also follows the -1/2-power-law scaling of the incompressible wake. The departure from this scaling given by the straight line begins at the same location, indicated by the gray arrow, at which $\delta_{1/2}(x)$ departed from its 1/2-power-law scaling due to the expansion wave interaction with the wake. The virtual origin obtained for the Mach 2 wake in figure 20a is

$$\left(\frac{x_0}{\vartheta}\right) = 25 \quad (19)$$

in good agreement with the value in (15) obtained from the velocity profile widths given by the solid symbols in figure 18a. The slope of the line in figure 20a gives the scaling constant as

$$c_u = 1.41. \quad (20)$$

In agreement with the results from the Mach 2 wake in §3.3.1, this is lower than the value in (10) found by Wygnanski *et al* (1986) in unforced incompressible wakes, and is indeed reasonably close to the value

$$c_u = 1.46 \pm 0.1 \quad (21)$$

found by Wygnanski *et al* in forced incompressible wakes. This can be seen in the log-log form in figure 20b, where the dashed and solid lines correspond, respectively, to the -1/2-power-law scalings with the scaling constants c_u for forced and unforced incompressible wakes. It thus appears clear that the Mach 2 wake, upstream of the location where the reflected expansion wave first intersects the wake, follows the same power-law scalings and scaling constants, for both $\delta_{1/2}(x)$

and $u_0(x)$, as are found in forced incompressible wakes.

Mach 3 wake

Analogous results for the Mach 3 wake are given in figure 21. Note that the data follow the classical $-1/2$ -power-law scaling up to the point where the expansion wave first intersects the wake, indicated by the gray arrow. The virtual origin was found to be

$$\left(\frac{x_0}{\vartheta} \right) = 12. \quad (22)$$

This is also in reasonable agreement with the value in (17) for velocity profile widths, relative to the much smaller corresponding value in (11) for incompressible wakes, and in fair agreement with (A.24). The scaling constant found from the slope in figure 21a is

$$c_u = 2.00. \quad (23)$$

and this is also comparable to the value in (10) found by Wygnanski *et al* for unforced, incompressible, bluff-body wakes. The log-log form in figure 21b verifies this, where the present data are shown together with lines giving unforced (solid line) and forced (dashed line) incompressible scalings of Wygnanski *et al*

It thus appears that unlike the Mach 2 wake, the Mach 3 wake upstream of the location where the reflected expansion wave first intersects the wake, follows the same power-law scalings and scaling constants, for both $\delta_{1/2}(x)$ and $u_0(x)$, as are found in unforced incompressible wakes.

4. Discussion

Section 3 presented results relevant to various scaling properties and associated scaling constants for supersonic, planar, turbulent, bluff-body wakes and compared these with corresponding results from incompressible wakes. It is apparent from figures 18 and 19 that the flow widths $\delta_{1/2}(x)$, measured using both visual and velocity widths in the Mach 2 and Mach 3 wakes, obey the $1/2$ -power-law scaling up to the point where the reflected expansion wave first intersects the wake. Also, from figures 20 and 21, the centerline velocity defect $u_0(x)$ over the same range of

downstream distances obeys the $-1/2$ -power-law scaling of incompressible wakes. At these values of (x/θ) , the local relative Mach numbers $M_r(x)$ in figure 17 are large enough in both the Mach 2 and Mach 3 wakes, in relation to the convective Mach numbers at which significant compressibility effects are seen in the supersonic turbulent mixing layers, that compressibility effects might be fully expected. In mixing layers, compressibility does not affect the power-law scaling, but reduces the scaling constant dramatically when $M_c > 0.2$. In the present wake experiments, the scaling constants appear to be more directly influenced by effects of forcing than by effects of compressibility. Such forcing appears to cause significant changes in the scaling constants, consistent with previous results from studies of forced incompressible turbulent wakes (*e.g.*, Wygnanski *et al* 198, Marasli *et al* 1992). Moreover, such forcing in the present wakes was seen in figures 8 and 9 to produce dramatic changes in the appearance of the large scale structure of the wake.

The principle effect of compressibility in the results presented thus far have to do with the ability of the locally induced forcing, created by the reflected expansion wave interactions with the flow, to propagate upstream along the wake centerline and thereby alter the scaling constants to the forced values. In the Mach 2 wake, the centerline Mach number $M_0(x)$ was subsonic at the point where the expansion wave first intersects the wake, and thus the periodic disturbance produced by the wave interaction with the wake could propagate upstream. In the Mach 3 wake, the point at which the expansion wave intersects the wake moved farther downstream, where the local centerline Mach number $M_0(x)$ was supersonic, and thus no subsonic path existed for the disturbances to propagate upstream.

In this section, certain additional considerations related to the effects of forcing on the scaling properties, and the resulting entrainment and mixing rates achieved by supersonic turbulent bluff-body wakes, will be discussed.

4.1 *Forcing effect due to wave interaction*

The local forcing produced by intersection of the reflected expansion wave with the

wake presumably occurs due to some type of interaction between the wake flow itself and the pressure field established by the wave intersection with the flow. That interaction may be as simple as the quasi-periodic pressure fluctuations created as the large scale vortical structures of the wake move through the expansion wave, however the available evidence is insufficient to be conclusive about the precise mechanism. At the wave intersection point, the forcing frequency will be automatically matched to the characteristic frequency $u_0(x)/\delta(x)$ of the large scale vortical structures in the wake, irrespective of the downstream location x at which the intersection occurs, since it is presumably the passage of the vortices past the stationary wave that is central to the forcing. Consequently, the local large scale vortices will always automatically “lock on” to the resulting forcing, in contrast to the externally introduced periodic disturbances that are typically used to force the growth rate of turbulent shear flows (*e.g.*, Oster & Wygnanski 1982, Roberts 1985, Roberts & Roshko 1985, Marasli *et al* 1992), for which the frequency must be tuned to the characteristic frequency $u_0(x)/\delta(x)$ of the large scale vortical structures. It is presumably this self-excited forcing mechanism in the supersonic wake that causes the departures of the $\delta(x)$ and $u_0(x)$ results from their power-law scalings past the point where the reflected expansion wave first intersects the wake.

In mixing layers, the increased growth of the flow is known to result from sympathetic interactions between the forcing frequency and the natural frequency of the large scale structures over a range of downstream locations. Results have shown that at downstream locations where the forcing frequency closely matches the local natural frequency $\Delta U/\delta(x)$ associated with the passage of large scale structures in the flow, the vortical structures lock onto the forcing frequency. This effect causes the flow width to increase much more rapidly than it normally would as it approaches the point where the natural frequency matches the forcing, and then to remain locked at roughly that width for some distance past this point, before subsequently returning to its natural growth.

Irrespective of the details of how the local forcing is produced by the expansion wave interaction with the wake, the resulting periodic disturbances propagate

downstream with the flow, and thus can affect the flow for some distance downstream of the wave intersection point. Based on the results from forced mixing layers and wakes noted above, the flow will remain receptive to these disturbances for a range of downstream distance past the wave intersection point, until the natural frequency of the wake becomes sufficiently mismatched to the forcing frequency. As a result, this receptive range will scale with the local outer scale $\delta(x)$ at the wave intersection point. Beyond this point, the wake becomes asymptotically unresponsive to the forcing, and thus will return to its natural growth. As can be seen in figures 18a and 19a, this can lead to a reduction in the wake width with increasing downstream distance. Such a reduction is clearly evident in the flow visualizations in figure 9. On the other hand, if a second interaction of the reflected expansion wave occurs before the wake returns to its natural width $\delta(x)$ given by the scaling laws (as is the case in figure 18a), then the process will repeat further downstream at a new, lower forcing frequency.

While these observations in the supersonic wake appear to be new, a somewhat related phenomenon has been reported in linear stability results by Umemura & Takihana (1997, 1998), who showed increased amplification of disturbances due to expansion wave intersection with the shear layers in the near field of wakes, and a corresponding acoustic feedback mechanism. Also related to this issue, Sato *et al* (1999) have reported results from experiments on growth rate enhancement in supersonic wakes by using a wall-mounted cavity to induce an acoustic disturbance on the wake.

4.2 Effects on scaling constants

The previous section discussed the effects of quasi periodic disturbances that propagate downstream from the wave intersection point. One of the principal effects of compressibility on the scaling constants in the wake flow upstream of the wave intersection point has to do with the ability of the forcing to propagate upstream, depending on the existence of any subsonic upstream path near the centerline of the wake. As noted above, the existence of such a path depends on the centerline Mach number $M_0(x) = M_\infty(x) - M_r(x)$, as indicated in figure 22. In the

present Mach 2 wake, the reflected expansion wave intersected the wake at a sufficiently small (x/θ), for which the centerline Mach number $M_0(x)$ was still subsonic. As a result, the forcing introduced by the expansion wave interaction with the wake propagated upstream to affect the entire wake, and consequently the wake displayed forced scaling constants upstream of the wave intersection point. In the Mach 3 wake, on the other hand, the reflected expansion wave interacted with the wake much farther downstream, where the centerline Mach number is supersonic, due to the shallower wave angles. As a result, no subsonic upstream path existed along which the local forcing produced by the wave interaction could propagate upstream, and the scaling constants for the Mach 3 wake displayed unforced values, as shown in figure 22.

4.3 Effects on entrainment and mixing

The present results have shown that self-induced excitation of the supersonic turbulent wake due to the reflected expansion wave interaction creates dramatic local changes in the growth rate and velocity decay rate within the wake due to forcing effects. This section examines whether or not these changes produce a resulting effect on the entrainment and mixing rates achieved by supersonic, planar, turbulent wakes.

The Appendix shows that, in incompressible planar turbulent wakes, the entrainment and mixing rate is determined by the growth rate $d\delta/dx$. This would suggest that, under entrainment-limited mixing conditions, an increase in the growth rate $d\delta/dx$ of the wake, such as that produced by the forcing effects due to expansion wave interaction with the flow, could potentially lead to an increase in the resulting molecular mixing rate. In principle, a similar mechanism for growth rate enhancement might also be applicable to other turbulent shear flows with a pronounced large scale vortical structure, including supersonic turbulent mixing layers. This suggests that mixing enhancement by expansion wave interactions with supersonic turbulent shear flows could be a potentially simple yet effective approach for passive mixing control in supersonic combustors. Moreover, unlike some methods previously suggested for mixing enhancement using shock waves, which

lead to total pressure losses, the present method based on expansion wave interactions only involves the Mach wave interactions, and thus no total pressure loss should be incurred.

Some caution must be exercised, however, before concluding that the growth rate enhancements seen here will necessarily lead to mixing enhancements. The scaling arguments above and in the Appendix apply to turbulent shear flows undergoing a natural “equilibrium” cascade. It is not assured that a turbulent shear flow that has been forced to increase its entrainment rate will necessarily preserve the same cascade process. In fact, there is indirect evidence that the present supersonic turbulent wakes may entrain more free stream fluid as their growth rate increases, and the de-entrain much or most of this fluid without molecularly mixing it. Figure 9 shows what appears to be precisely this phenomenon. The pronounced “zig-zag” structures seen in the top panel, for instance, show a dramatic increase in the amount of entrained (black) free stream fluid within the wake. However this fluid is clearly not undergoing any natural turbulent cascade process to become mixed with other fluid in the wake. In fact, it is apparent that this entrained fluid is not participating in a turbulent cascade process at all; it is merely being temporarily carried with the wake. Further downstream, where the wake begins to return to its natural growth rate (see figure 19a) the wake in figure 9 appears to do this by expelling much of this entrained fluid out of the wake. Near the right edge of the picture, the wake appears to return to its natural cascade process, in which entrained fluid immediately begins the cascade process down to the length scale λ_v to be subsequently mixed at the molecular scale with other fluid already in the wake. The key point is that the limited evidence available here on this matter suggests that the wake is brought temporarily out of its natural “equilibrium” cascade by the forcing, only to return to its natural equilibrium by expelling most of the additional fluid it entrained as a result of the forcing. That would suggest an increase in entrainment rate only, but little or no change in the mixing rate. Indeed, the limited measurements relevant to this issue in incompressible, forced, turbulent mixing layers suggests that this may in fact be the case.

4.4 Growth rate vs. relative Mach number

Figure 23 shows the measured values for the scaling constant c_s , obtained from (7) and normalized by the value $(c_s)_0$ in unforced incompressible wakes by Wygnanski *et al* (1986), against the relative Mach number M_r , for both the Mach 2 and Mach 3 wakes. The interest here is to determine if the relative Mach number has a similar effect on the growth rate scaling constant in supersonic planar turbulent wakes as it does in supersonic planar turbulent mixing layers. In the supersonic mixing layer, the corresponding result for $c_s/(c_s)_0$ shows a large reduction with increasing M_r , as was noted in §1.1. It is apparent from the results in figure 23 that no such reduction occurs in the supersonic wake. While the applicability of the $(c_s)_0$ value from unforced incompressible wakes may be questioned in view of the observed effects of forcing in supersonic wakes, this does not change the fact the $c_s/(c_s)_0$ values show no significant reduction with increasing M_r over a range where analogous results in mixing layers show a reduction of nearly 70%. Consistent with results found elsewhere in this study, we conclude that compressibility effects manifest themselves very differently in supersonic turbulent bluff-body wakes than they do in supersonic mixing layers.

5. Conclusions

Major conclusions drawn from the present experimental study of compressibility effects on entrainment and mixing in the near- and far-fields of supersonic, planar, turbulent, bluff-body wakes can be summarized as follows:

1. The classical vortex street-like large scale structure of incompressible, planar, turbulent wakes is recovered in the far-field of the present supersonic wakes where the relative Mach number $M_r(x)$ has decreased to around 0.4.
2. A classical supersonic base flow region exists immediately behind the bluff body. The mass injection rate into this base flow region affects its size and alters the expansion fan and recompression waves, and thus affects the virtual origin (x_0/ϑ) of the far-field similarity scalings of the resulting wake.

3. Mean velocity profiles in the wake far-field are self-similar when scaled by the local flow width and mean centerline velocity defect, even after the reflected expansion waves and shocks interact with the wake.
4. The flow width and mean centerline velocity defect in the supersonic wake follow the classical $(x/\vartheta)^{1/2}$ and $(x/\vartheta)^{-1/2}$ scalings of incompressible planar turbulent wakes. The virtual origin (x_0/ϑ) of these scalings shifts downstream in supersonic wakes due to the base flow region.
5. Interactions between reflected expansion waves and the wake create a local self-induced periodic forcing that is inherently matched to the local natural frequency of the wake vortices, leading to “lock on” of the vortical structures to this forcing. The effect is similar to the response of incompressible turbulent mixing layers and wakes to imposed forcing, but in the supersonic wake the forcing is self-induced.
6. Due to this self-induced forcing mechanism, the local growth rate and velocity decay rate of the wake increase dramatically immediately downstream of the point where the reflected expansion wave intersects the wake. Sufficiently far downstream of the wave intersection point, the wake returns to its natural growth and decay rates.
7. Upstream of the point where the reflected near-field expansion wave first intersects the wake, the measured far-field scaling constants c_δ and c_u of the wake display either the forced or unforced values from incompressible turbulent wakes, depending on whether the local centerline Mach number provides a subsonic path for the wave-induced forcing to propagate upstream.
8. Though the entrainment rate increases dramatically due to this self-induced

forcing, the available evidence suggests that the mixing rate does not increase. As the wake returns to its natural growth rate, much of the additionally entrained free stream fluid appears to be detrained.

9. The effects of compressibility in confined supersonic, planar, turbulent, bluff-body wakes are significantly different from those previously documented in supersonic, planar, turbulent mixing layers.

Appendix

This Appendix discusses certain fundamental properties of planar turbulent wakes that are used throughout this investigation. These consists of specific scaling properties of planar turbulent wakes, predictions of virtual origins for both incompressible and supersonic wakes, and an analysis of the entrainment and mixing rate in planar turbulent wakes.

A.1 *Scaling of incompressible planar turbulent wakes*

Classical similarity arguments, when applied to the thin-layer forms of the mass and momentum conservation equations together with the “far-wake approximation” $u \ll U_\infty$, lead to scaling laws for the outer variables $u_0(x)$ and $\delta(x)$ in incompressible planar turbulent wakes as

$$(u_0/U_\infty) = c_u (x/\vartheta)^{-1/2} \quad (A.1a)$$

$$(\delta/\vartheta) = c_\delta (x/\vartheta)^{1/2}, \quad (A.1b)$$

where u_0 and δ are defined in figure 1. For unforced wakes, values for the universal scaling constants are found to be $c_\delta \approx 0.29$ and $c_u \approx 1.70$ (e.g., Wygnanski *et al* 1986). Momentum conservation implies that ϑ in (4) will be invariant with x when $dp/dx = 0$. In the far-wake this becomes

$$\vartheta \approx \int_{-\infty}^{+\infty} \frac{u(y)}{U_\infty} dy, \quad (A.2)$$

and on substituting from (A.1a,b) requires that the scaling constants c_δ and c_u in the far wake must satisfy

$$c_u \cdot c_\delta = \frac{1}{I} , \quad (A.3)$$

where

$$I \equiv \int_{-\infty}^{+\infty} f(\eta) d\eta \quad (A.4)$$

with

$$f(\eta) \equiv \frac{u(\eta)}{u_0(x)} \quad (A.5a)$$

$$\eta \equiv \frac{y}{\delta(x)} . \quad (A.5b)$$

Wygnanski *et al* (1986) fit the similarity profile shape $f(\eta)$ in figure 16 as

$$f(\eta) = \exp(-0.693\eta^2 - 0.056\eta^4) , \quad (A.6)$$

which from (A.3) then requires

$$c_u \cdot c_\delta = 0.485 . \quad (A.7)$$

This agrees relatively well with the value of 0.506 ± 0.002 obtained by Wygnanski *et al* (1986).

A.2.2 Reynolds numbers

The local inner length scale $\lambda_v(x)$ and outer length scale $\delta(x)$ are related at any downstream location x in a turbulent shear flow as $\lambda_v/\delta \approx 11.2 Re_\delta^{-3/4}$, where

$$Re_\delta \equiv \frac{u_0 \delta}{v} \quad (A.8)$$

is the local outer-scale Reynolds number, and the scaling constant is from Buch & Dahm (1998) and Dahm & Southerland (1999). From (A.1a,b), Re_δ is invariant with downstream distance as

$$Re_\delta = c_\delta c_u \frac{U_\infty \vartheta}{v} , \quad (A.9)$$

where it is common to define

$$Re_\vartheta \equiv \frac{U_\infty \vartheta}{v} \quad (A.10)$$

as the Reynolds number based on momentum thickness ϑ and the free stream velocity U_∞ . From (A.9) and (A.10), together with (A.7), it follows that $Re_\delta \approx \frac{1}{2} Re_\vartheta$.

A.2 Virtual origin x_0 for incompressible bluff-body wakes

As shown schematically in figure A.1, the scaling for such turbulent wakes is based on the fact that the drag D is the only invariant of the resulting flow. As a consequence, it remains relevant to the momentum transport process within the wake at all downstream distances, while the relative effect of all other aspects of the source becomes smaller with increasing downstream distance x . In the “far field” of the wake, the drag is the only remaining dynamically relevant aspect of the source, and the scalings for $u_0(x)$ and $\delta(x)$ are then determined entirely by the downstream distance, the net drag, the fluid density, and the free stream velocity. In effect, the wake source is replaced by a singularity that removes momentum from the free stream at the same rate as the actual source. However, if the downstream coordinate x is to denote the distance measured from the actual wake source, then the shift x_0 in the position of the equivalent point singularity relative to the actual source must be accounted for. In this section, a procedure of that gives the value of this “virtual origin” is shown for incompressible planar bluff-body wakes.

Figure A.1a shows a typical bluff-body wake generated by a body with frontal dimension d . The location of the equivalent point singularity in figure A.1b relative to the coordinate origin $x = 0$ is the “virtual origin”, denoted x_0 . The wake generated by the actual source can be related to the corresponding ideal wake by taking x_0 into account. This simply requires that the power-law scalings in (A.1a,b) must be modified to account for the shift due to the virtual origin as

$$\frac{u_0}{U_\infty} = c_u \left(\frac{x - x_0}{\vartheta} \right)^{-\frac{1}{2}} \quad (\text{A.11a})$$

$$\frac{\delta}{\vartheta} = c_\delta \left(\frac{x - x_0}{\vartheta} \right)^{\frac{1}{2}} \quad (\text{A.11b})$$

It is a simple matter to find the virtual origin x_0 from experimental data by extrapolating in a plot of $(\delta/\vartheta)^2$ or $(u_0/U_\infty)^2$ against (x/ϑ) .

However, it is also possible to obtain a theoretical estimate for x_0 by a simple

procedure. Define the initial width δ_0 of the wake as indicated in figure A.1b, namely

$$\delta_0 = \delta(x_0) . \quad (A.12)$$

As figure A.1 suggests, δ_0 should be proportional to the frontal dimension d as

$$\delta_0 \equiv \alpha d , \quad (A.13)$$

the proportionality factor α will depend (weakly) on the body shape via the details of the boundary layer separation process. For most shapes, we can expect $\alpha \approx 1.5$, and for essentially all body shapes we can safely expect $1 \leq \alpha < 2$. Substituting in (A.11b) then gives

$$x_0 = \frac{\alpha^2 d^2}{\vartheta c_\delta^2} , \quad (A.14)$$

Introducing the drag coefficient C_D of the wake generator, namely

$$C_D = \frac{D}{\frac{1}{2} \rho U_\infty^2 d} , \quad (A.15)$$

and noting that

$$\vartheta = \frac{1}{2} C_D d , \quad (A.16)$$

then gives the virtual origin for incompressible, planar, turbulent, bluff-body wakes as

$$\frac{x_0}{\vartheta} = \left(\frac{2}{c_\delta} \right)^2 \left(\frac{\alpha}{C_D} \right)^2 . \quad (A.17)$$

A similar result can be obtained for axisymmetric wakes.

Note that C_D and α in (A.17) are closely related via free streamline theory, and depend on the bluff-body shape. For instance, for a circular cylinder $C_D \approx 1$ for $Re > 10^3$, and taking $\alpha \approx 1.5$ and using $c_\delta = 0.28$ from Wygnanski *et al* (1986), the value of x_0/ϑ from (A.17) becomes

$$\frac{x_0}{\vartheta} = -123 , \quad (A.18)$$

which agrees very well with the experimental value of $x_0/\vartheta \approx -128$ reported by Wygnanski *et al*.

A.3 Virtual origin x_0 for supersonic bluff-body wakes

To extend the above result to compressible turbulent wakes, additional account must be taken of the more complicated geometry of the near-field recompression region on the virtual origin x_0 , as indicated in figure A.2 (see also figures 4-6). In this case, the initial width δ_0 of the wake is determined from the width of the “neck” formed by the recompression, which is shifted downstream of the actual wake source by the length x_R of the recompression region. If the coordinate x again measures the distance from the actual wake source, then the location x_0 of the equivalent point singularity is given by

$$x_0 = x_R - s_0 , \quad (A.19)$$

where s_0 is the location of the point singularity relative to the neck. In direct analogy with (A.14), s_0 is obtained as

$$s_0 = \frac{\alpha_R^2 d^2}{c_\delta^2 \vartheta} , \quad (A.20)$$

where α_R is now the proportionality constant between the neck width δ_0 and the size d of the wake generator. When the mass injection rate m_0 at the wake source is sufficiently small for its effect on δ_0 to be neglected, as is presumed to be the case here, then

$$\delta_0 \approx d / 4 , \quad (A.21)$$

as suggested by figure 6, giving $\alpha_R \approx 0.25$. For large injection rates, the neck width δ_0 will increase to accommodate the mass flow m_0 , and this will lead to an increase in α_R ; evidence of this can be seen in figure 5, where at large injection rates δ_0 becomes comparable to d .

The length x_R of the recompression region in figure A.2 (see also figure 4) is determined by the turning angle associated with the expansion fan, which in turn is set by the pressure ratio (p_0/p_∞), where p_0 is the base pressure and p_∞ the free stream pressure. When the base pressure is relatively unaffected by mass injection into the base region, then the turning angle suggested by figure 6 is roughly 20° . This gives

$$x_R \approx 1.4d . \quad (A.22)$$

Combining (A.19) with (A.20) and (A.22), together with (A.16), then gives the virtual origin for the supersonic wake as

$$\frac{x_0}{\vartheta} = \frac{1}{C_D} \left(2.8 - \frac{1}{4c_\delta^2 C_D^2} \right) , \quad (A.23)$$

where again taking $C_D \approx 1$ and $c_\delta \approx 0.29$ would give

$$\frac{x_0}{\vartheta} \approx 0 . \quad (A.24)$$

This result must be viewed as qualitative only, given the approximations involved. However it demonstrates that the virtual origin for compressible wakes is shifted far downstream relative to that for incompressible wakes in (A.17) and (A.18), in agreement with the results in §3, and gives some insights into the reasons for this shift.

A.4 Entrainment rate

As noted in §1, the mixing process in fully turbulent shear flows is “entrainment-limited”, and the mixing rate is therefore determined entirely by the entrainment rate. The entrainment rate, in turn, is set by the local outer variables $\delta(x)$ and $u_0(x)$, and thus depends on the power-law scalings and the associated scaling constants c_δ and c_u , as shown below.

The mass flux across any lateral plane is given by

$$m(x) \equiv \int_{-\infty}^{+\infty} \rho U(y) dy . \quad (A.25)$$

From the definition of the defect velocity $u(y)$, namely

$$U(y) \equiv U_\infty - u(y) , \quad (A.26)$$

this can be written as

$$m(x) \approx \rho_\infty U_\infty \delta(x) - \rho_\infty u_0(x) \delta(x) I , \quad (A.27)$$

where I is given in (A.4). Substituting for $\delta(x)$ and $u_0(x)$ from (A.1a,b) and noting that the power law scalings cancel in the second term on the right, it becomes apparent that the entrainment rate dm/dx is

$$\frac{dm}{dx} \sim \frac{d}{dx} [\rho_\infty U_\infty \delta(x)] , \quad (A.28)$$

from which it is evident that the growth rate $d\delta/dx$ determines the entrainment and mixing rate in planar turbulent wakes.

References

- Alber I.E. & Lees, L. (1968) Integral theory for supersonic turbulent base flows. *AIAA J.* **6**, 1343-1351.
- Amatucci, V.A., Dutton, J.C., Kuntz, D.W. & Addy, A.L. (1992) Two-stream, supersonic, wake flow field behind a thick base. Part I: General features. *AIAA J.* **30**, 2039-2046.
- Barre, S., Quine, C. & Dussauge, J.P. (1994) Compressibility effects on the structure of supersonic mixing layers: experimental results. *J. Fluid Mech.* **259**, 47-78.
- Berger, S.A. (1971) Laminar Wakes. Elsevier, New York.
- Bogdanoff, D.W. (1982) Compressibility effects in turbulent shear layers. *AIAA J.* **21**, 926-927.
- Bonnet, J.P., Jayaraman, V. & de Roquefort, T.A. (1984) Structure of a high-Reynolds-number turbulent wake in supersonic flow. *J. Fluid Mech.* **143**, 277-304.
- Bonnet, J.P. & Chaput, E. (1986) Large-scale structure visualization in a high Reynolds number, turbulent flat-plate wake at supersonic speed. *Expts. Fluids* **4**, 350-356.
- Buch, K.A. & Dahm, W.J.A. (1998) Experimental study of the fine-scale structure of conserved scalar mixing in turbulent flows. Part 2. $Sc \approx 1$. *J. Fluid Mech.* **364**, 1 - 29.
- Chen, J.H., Cantwell, B.J. & Mansour, N.N. (1990) The effect of Mach number on the stability of a plane turbulent wake. *Phys. Fluids A* **2**, 984-1004.

Chinzei, N., Masuya, G., Komuro, T., Murakami, A. & Kudou, K. (1986) Spreading of two-stream supersonic turbulent mixing layers. *Phys. Fluids* **29**, 1345-1347.

Cimbala, J.M., Nagib, H.M. & Roshko A. (1988) Large structure in the far wakes of two-dimensional bluff bodies. *J. Fluid Mech.* **190**, 265-298.

Clemens, N.T. (1991) An experimental investigation of scalar mixing in supersonic turbulent shear layers. HTGL Report No. T-274, Stanford University.

Clemens, N.T. & Mungal, M.G. (1991) A planar Mie scattering technique for visualizing supersonic mixing flows, *Expts. Fluids* **11**, 175-185.

Clemens, N. T. & Mungal, M. G. (1992a) Two- and three-dimensional effects in the supersonic mixing layer. *AIAA J.* **30**, 973-981.

Clemens, N.T. & Mungal, M.G. (1992b) Effects of sidewall disturbances on the supersonic mixing layer. *J. Propulsion and Power* **8**, 249-251.

Clemens, N.T. & Mungal, M.G. (1995) Large-scale structure and entrainment in the supersonic mixing layer. *J. Fluid Mech.* **284**, 171-216.

Clemens, N.T. & Smith, M.F. (1996) Observations of supersonic flat plate wake transition. *AIAA J.* **36**, 1328-1330.

Dahm, W.J.A. & Southerland, K.B. (1999) Quantitative flow visualization via fully-resolved four-dimensional spatio-temporal imaging. Chapter 11 in Flow Visualization: Techniques and Examples, (A. Smits and T.T. Lim, Eds.), 231 – 258, Imperial College Press, London.

Dimotakis, P.E. (1991) Turbulent free shear layer mixing and combustion. In High-Speed Flight Propulsion Systems (S.N.B. Murthy & E.T. Curran, Eds.) of Progress in Aeronautics & Astronautics, Vol. 137, 265-340. AIAA, Washington, D.C.

Elliott, G.S. & Samimy, M. (1990) Compressibility effects in free shear layers. *Phys. Fluids A* **2**, 1231-1240.

Elliott, G.S., Samimy, M. & Arnette, S.A. (1995) The characteristics and evolution of large-scale structures in compressible mixing layers. *Phys. Fluids A* **7**, 864-876.

Goebel, G.S. & Dutton, J.C. (1991) Experimental study of compressible turbulent mixing layers. *AIAA J.* **29**, 538-546.

Gruber, M.R., Messersmith, N.L. & Dutton, J.C. (1993) Three-dimensional velocity field in a compressible mixing layer. *AIAA J.* **31**, 2061-2067.

Hall, J.L., Dimotakis, P.E. & Rosemann, H. (1993) Experiments in nonreacting compressible shear layers. *AIAA J.* **31**, 2247-2254.

Herrin, J.L. & Dutton, J.C. (1994) Supersonic base flow experiment in the near wake of a cylindrical afterbody. *AIAA J.* **32**, 77-83.

Lachney, E.R. & Clemens, N.T. (1998) PLIF imaging of mean temperature and pressure in a supersonic bluff wake. *Expts. Fluids* **24**, 354-363.

Lee, S., Lele, S.K. & Moin, P. (1991) Eddy shocklets in decaying compressible turbulence. *Phys. Fluids A* **3**, 657-664.

Lees, L. (1964) Hypersonic wakes and trails. *AIAA J.* **2**, 417-428.

Lykoudis, P. (1966) Review of hypersonic wake studies. *AIAA J.* **4**, 577-590.

Marasli, B., Champagne, F.H. & Wygnanski, I. (1992) Effect of travelling waves on the growth of a plane turbulent wake. *J. Fluid Mech.* **235**, 511-528.

McIntyre, S.S. & Settles G.S. (1991) Optical experiments on axisymmetric compressible turbulent mixing layers. *AIAA Paper No. 91-0623*, 29th Aerospace Sciences Meeting, AIAA, Washington, D.C.

Nakagawa, M. & Dahm, W.J.A. (1999) Compressibility effects on entrainment and mixing in supersonic planar turbulent wakes. *AIAA Paper No. 99-3582*, 30th AIAA Fluid Dynamics Conference, AIAA, Washington, D.C.

Nakagawa, M. & Dahm, W.J.A. (2000) Mach number effects on entrainment and mixing in supersonic planar turbulent wakes. *AIAA Paper No. 2000-0664*, 38th AIAA Aerospace Sciences Meeting & Exhibit, AIAA, Washington, D.C.

Noack, B.R. & Eckelmann, H. (1994) A global stability analysis of the steady and periodic cylinder wake. *J. Fluid Mech.* **270**, 297-330.

Olsen, M.G. & Dutton, J.C. (1999) Planar velocity measurements in a weakly compressible mixing layer. *AIAA Paper 99-3584*, 30th AIAA Fluid Dynamics Conference, AIAA, Washington, D.C.

Oster, D. & Wygnanski, I. (1982) The forced mixing layer between parallel streams. *J. Fluid Mech.* **123**, 91-130.

Papageorgiou, D.T. & Smith, F.T. (1989) Linear instability of the wake behind a flat plate placed parallel to a uniform stream. *J. Fluid Mech.* **208**, 67-89.

Papamoschou, D. & Roshko A. (1988) The compressible turbulent shear layer: an experimental study. *J. Fluid Mech.* **197**, 453-477.

Papamoschou, D. (1991) Structure of the compressible turbulent shear layer. *AIAA J.* **29**, 680-681.

Papamoschou, D. (1992) Effect of three-dimensionality on compressible mixing. *J. Propulsion* **8**, 247-249.

Pope, A. & Goin, K.L. (1965) High-Speed Wind Tunnel Testing. John Wiley & Sons, New York.

Roberts, F.A. (1985) Effects of a periodic disturbance on structure and mixing in turbulent shear layers and wakes. Ph.D thesis, California Institute of Technology.

Roberts, F.A. & Roshko, A. (1985) Effects of periodic forcing on mixing in turbulent shear layers and wakes. *AIAA Paper No. 85-0570*, Shear Flow Control Conference, AIAA, Washington, D.C.

Samimy, M. & Elliott, G.S. (1990) Effects of compressibility on the characteristics of free shear layers. *AIAA J.* **28**, 439-445.

Samimy, M., Reeder, M.F. & Elliott, G.S. (1992) Compressibility effects on large structures in free shear flows. *Phys. Fluids A* **4**, 1251-1258.

Sato, N., Imamura, A., Shiba, S., Takahashi, S., Tsue, M. & Kono, M. (1999) Advanced mixing control in supersonic airstream with a wall-mounted cavity. *J. Propulsion and Power* **15**, 358-360.

Umemura, A., Miura, K. & Takada, K. (1996) Suppression of embedded shocks in supersonic free-shear-layer structures. *Shock Waves* **6**, 167-175.

Umemura, A. & Takihana, Y. (1997) Instabilities of confined, supersonic, double shear layer flow. *Trans. Japan Soc. Aero. Space Sci.* **45**, 564-574.

Umemura, A. & Takihana, Y. (1998) Nonlinear instabilities leading to rapid mixing and combustion in confined supersonic double-shear-layer flow. *Proc. Comb. Inst.* **27**, 2135-2142, The Combustion Institute, Pittsburgh.

Urban, W.D. & Mungal, M.G. (1997) Planar velocity measurements in compressible mixing layers. *AIAA Paper No. 97-0757*, 35th Aerospace Sciences Meeting & Exhibit, AIAA, Washington, D.C.

Urban, W.D., Watanabe, S. & Mungal, M.G. (1998) Velocity field of the planar shear layer: compressibility effects. *AIAA Paper No. 98-0697*, 36th Aerospace Sciences Meeting & Exhibit, AIAA, Washington, D.C.

Wygnanski, I., Champagne, F. & Marasli, B. (1986) On the large-scale structures in two-dimensional, small-deficit, turbulent wakes. *J. Fluid Mech.* **168**, 31-71.

Zeman, O. (1992) Similarity in supersonic mixing layers. *AIAA J.* **30**, 1277-1283.

		$M_\infty \approx 2.0$	$M_\infty \approx 3.0$		
A^*	[mm ²]	8.99×38.4	8.99×38.4		
A_{exit}	[mm ²]	15.2×38.4	15.2×38.4		
L	[mm]	63.5	71.1		
p_0	[kPa]	653	653		
T_0	[K]	283	283		
p_{exit}	[kPa]	83.3	103	20.4	20.2
T_{exit}	[K]	167	177	117	122
U_{exit}	[m/s]	482	461	577	569
M_{exit}	—	1.86	1.73	2.66	2.57
Re_L	—	4.8×10^6		2.9×10^6	
ϑ	[mm]	0.4		0.55	
Re_ϑ	—	31,000		23,000	

Table 1. Supersonic nozzle dimensions and experimental flow conditions.

	$M_\infty << 1$		$M_\infty = 2$		$M_\infty \approx 3$	
	unforced	forced	$\delta_{1/2}$	u_0	$\delta_{1/2}$	u_0
$(x_0/\vartheta)_{\text{visual}}$	—	—	-31	25	-90	12
(x_0/ϑ)	-128	-128	22	25	5	12
c_δ	0.27	0.35 ± 0.03	0.39	—	0.26	—
c_u	1.88	1.46 ± 0.1	—	1.41	—	2.00

Table 2. Summary of scaling constants resulting from PLMS visualizations and pressure measurements in §3 for the supersonic planar turbulent wake, showing scaling constants for incompressible planar turbulent wakes by Wygnanski *et al.* (1986) for comparison.

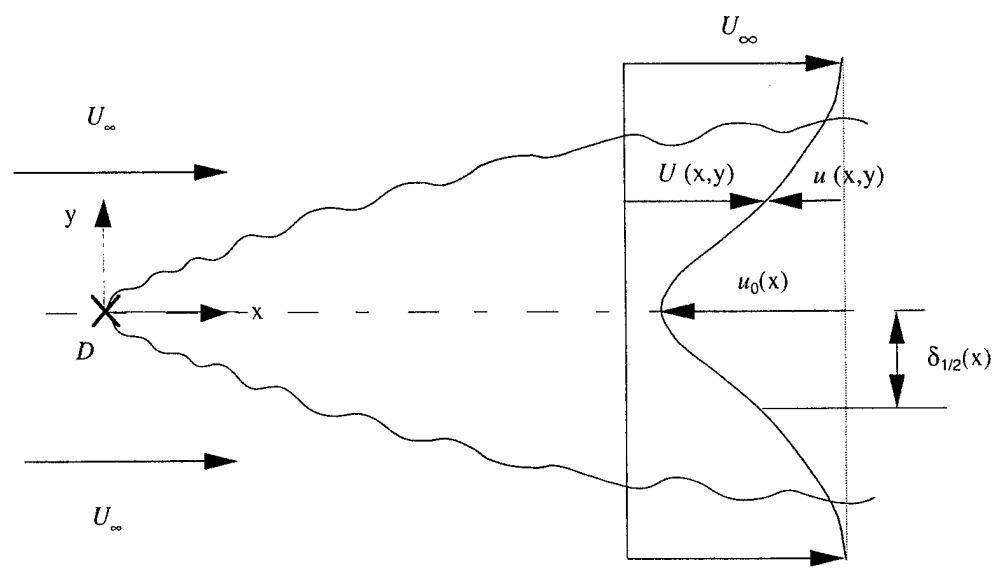


Figure 1. Sketch of the planar turbulent wake with definitions of variables.

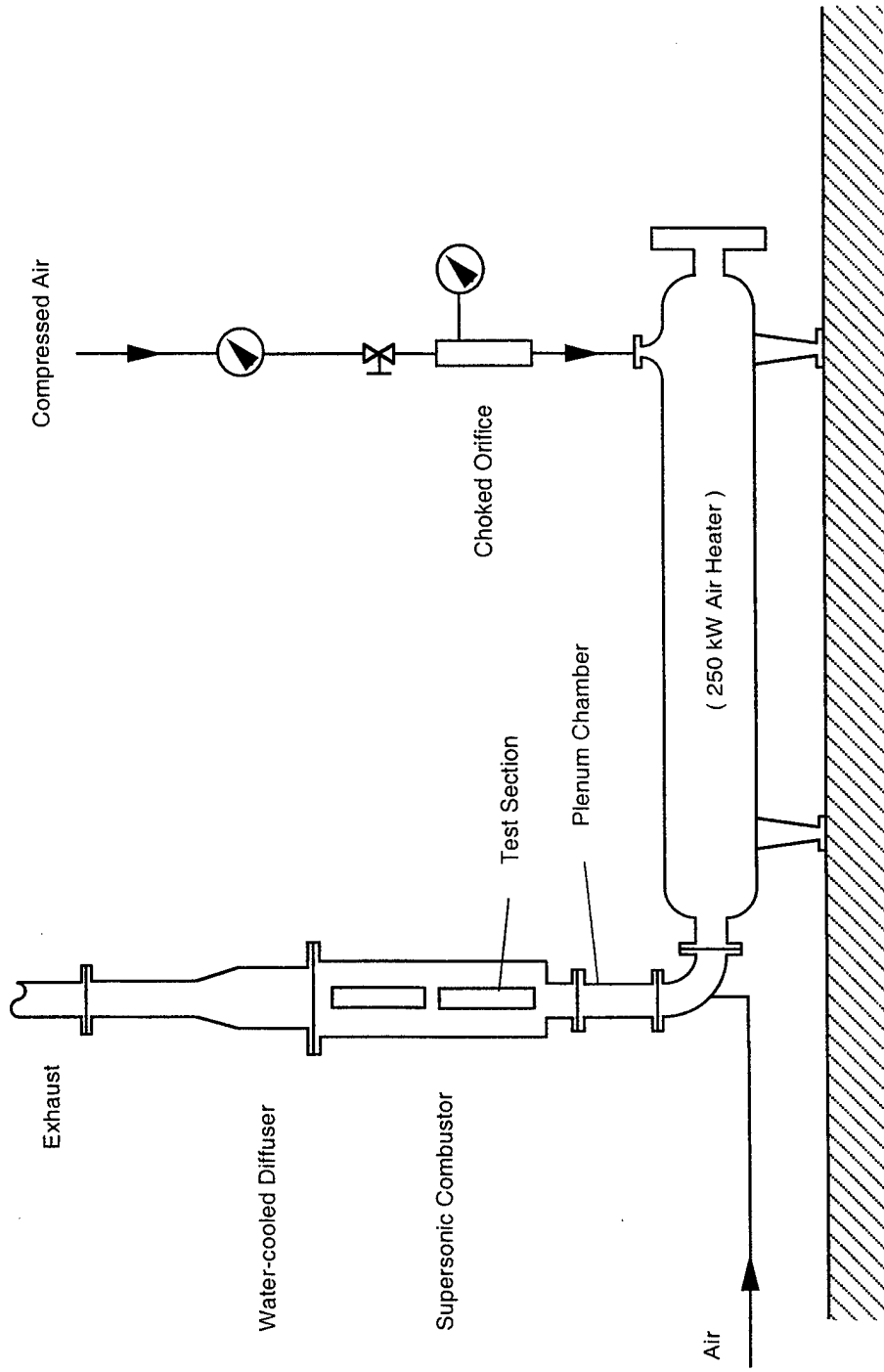


Figure 2. Schematic of the Michigan Supersonic Mixing and Combustion Facility, showing the test section, the electrical heater, and other major components of the flow control system.

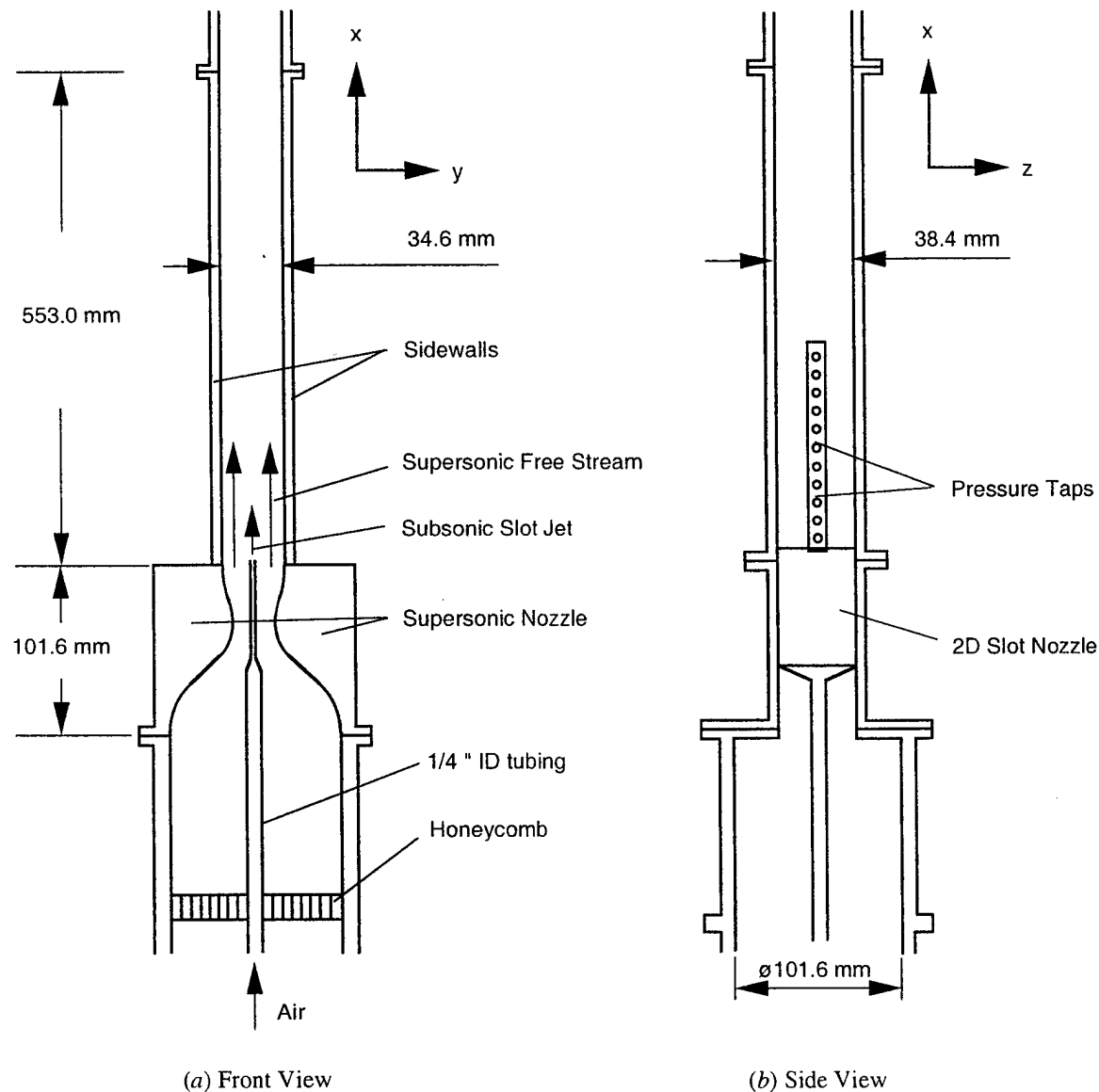


Figure 3. Schematic of the supersonic nozzle, the test section, and the subsonic slot nozzle.

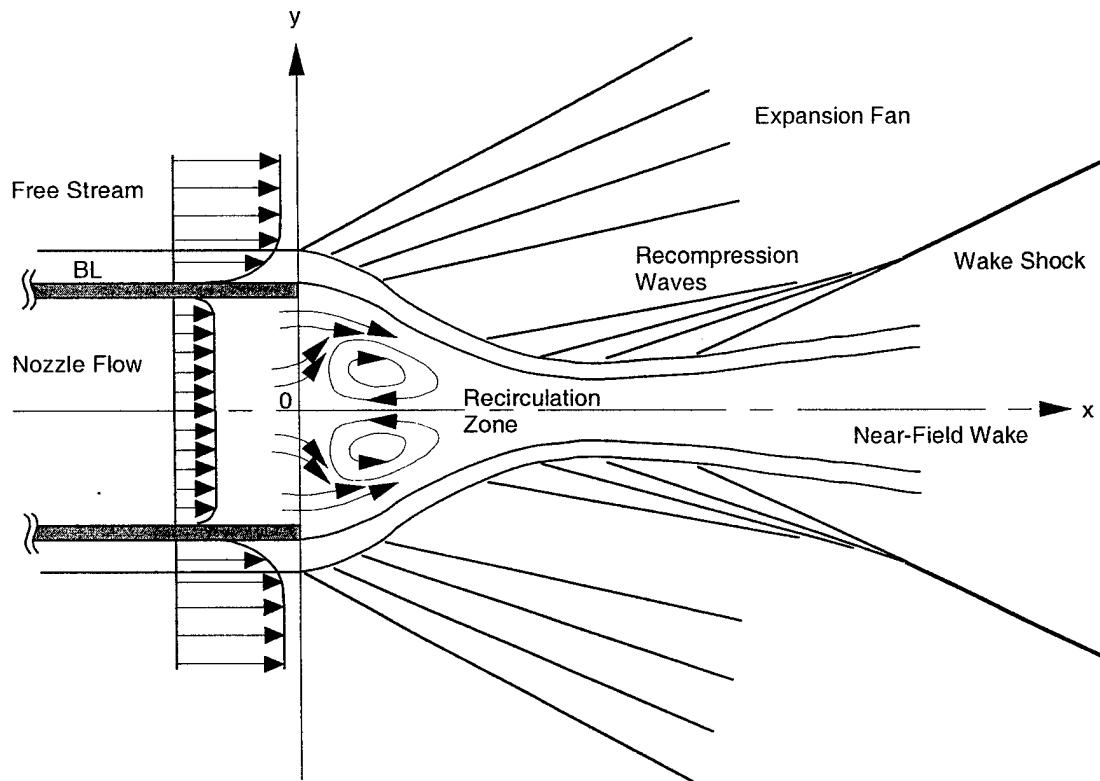


Figure 4. Schematic indicating major features of the near-field supersonic wake just beyond slot jet exit, showing wake expansion and recompression waves above wake centerline, as well as coupling between slot jet flow rate and base flow structure and size.

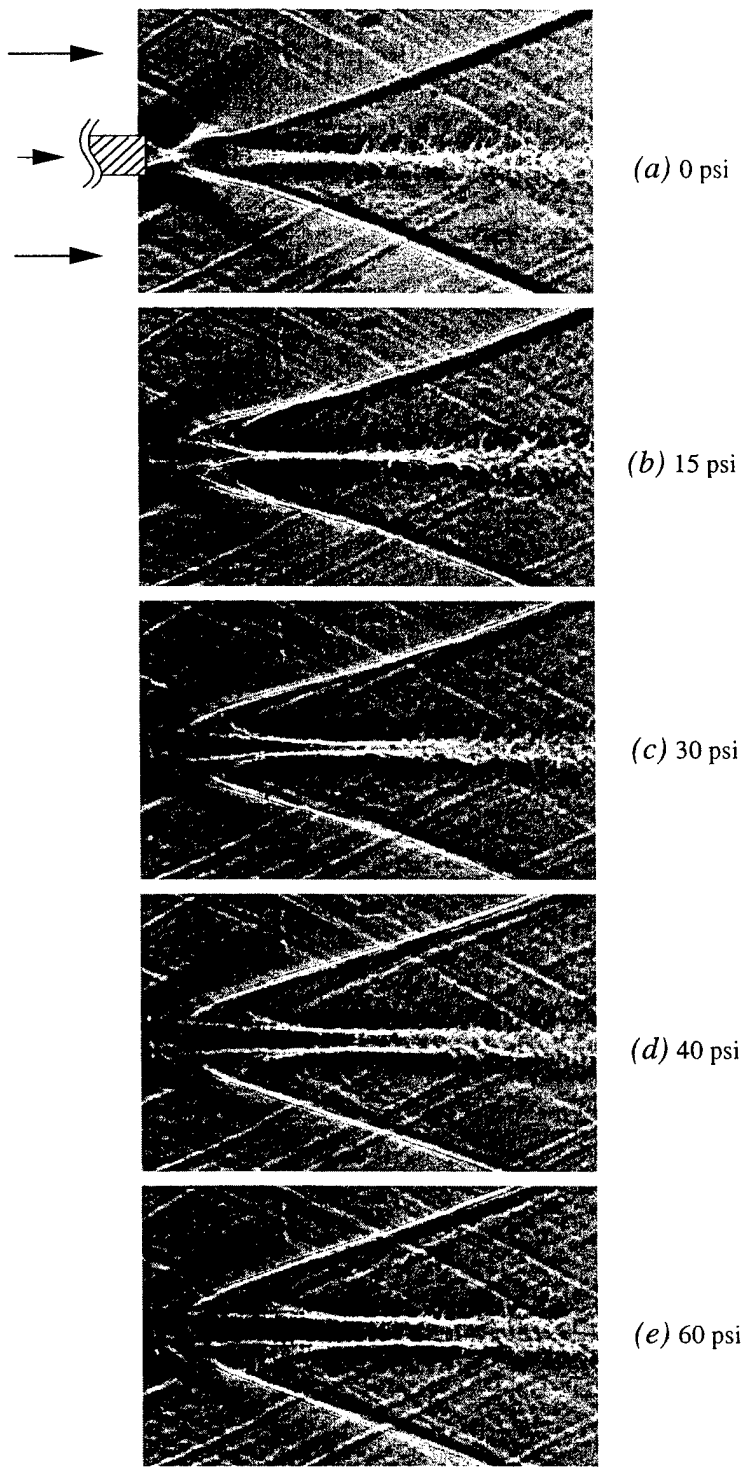


Figure 5. Shadowgraph images for the Mach 2 wake showing effect of slot jet flow rate as determined by jet supply pressure on wave pattern, structure, and near-field length with 4° diverging sidewalls. The gas issued from the slot jet is propane.

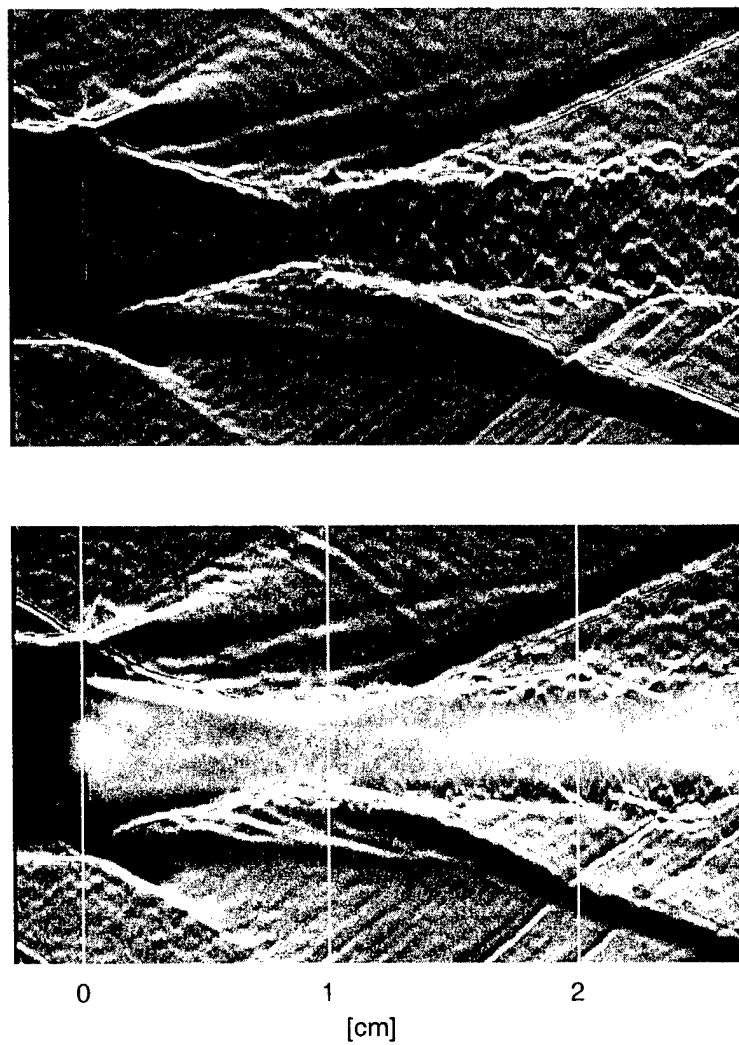


Figure 6. Shadowgraph images of near-field region (*top*) with typical PLMS image superimposed (*bottom*) for the Mach 2 wake, showing base flow region and early self-similar wake region. See corresponding PLMS images in figure 7.

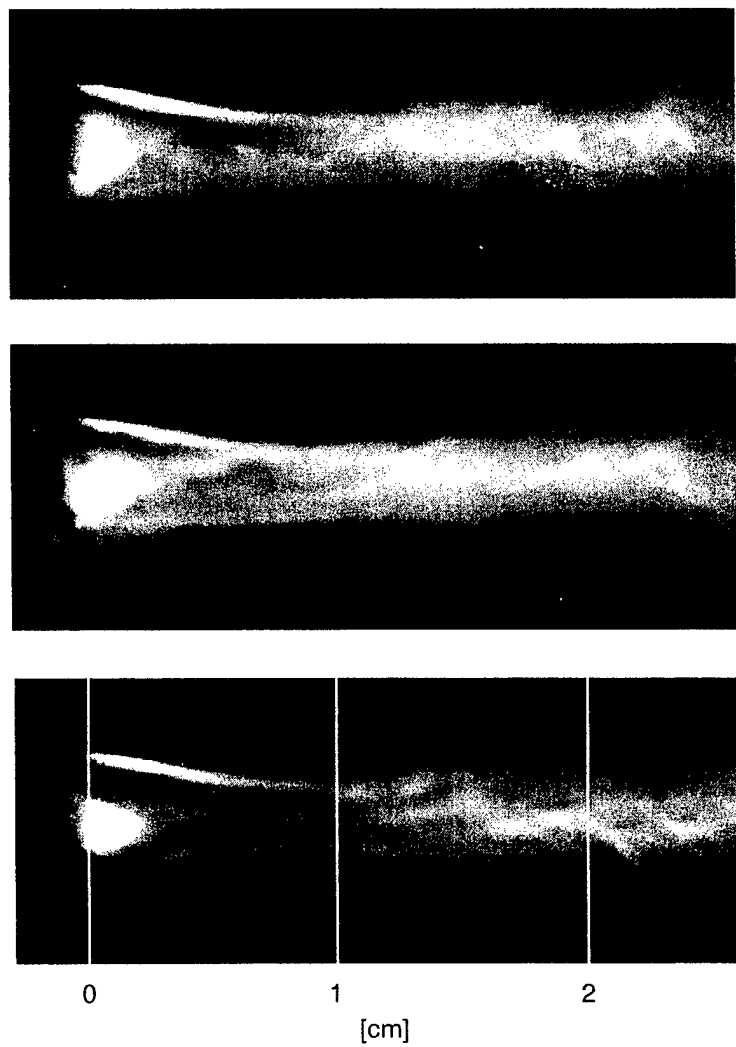


Figure 7. Typical instantaneous PLMS images in the near-field region for the Mach 2 wake., showing base flow region and early self-similar wake region. Note that no organized vortical structures is apparent up to the right edge of the field of view.

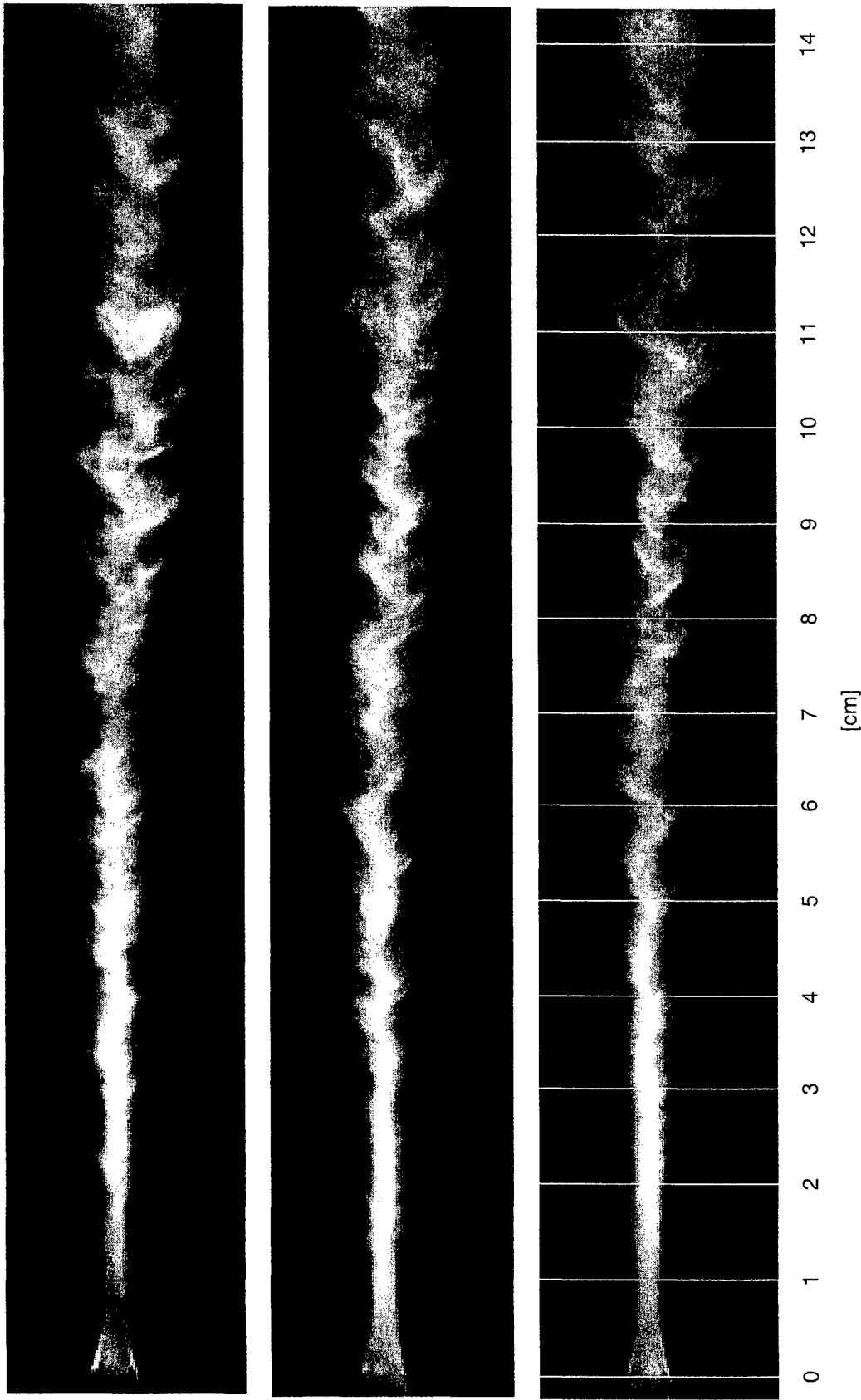


Figure 8. Typical instantaneous PLMS images for the Mach 2 wake, showing development of characteristic vortex street-like large scale structures in far-field region, with alternating signs of circulation, and the lack of any apparent structures immediately downstream of base flow region (also see figure 7), where the relative Mach number remains comparatively high.

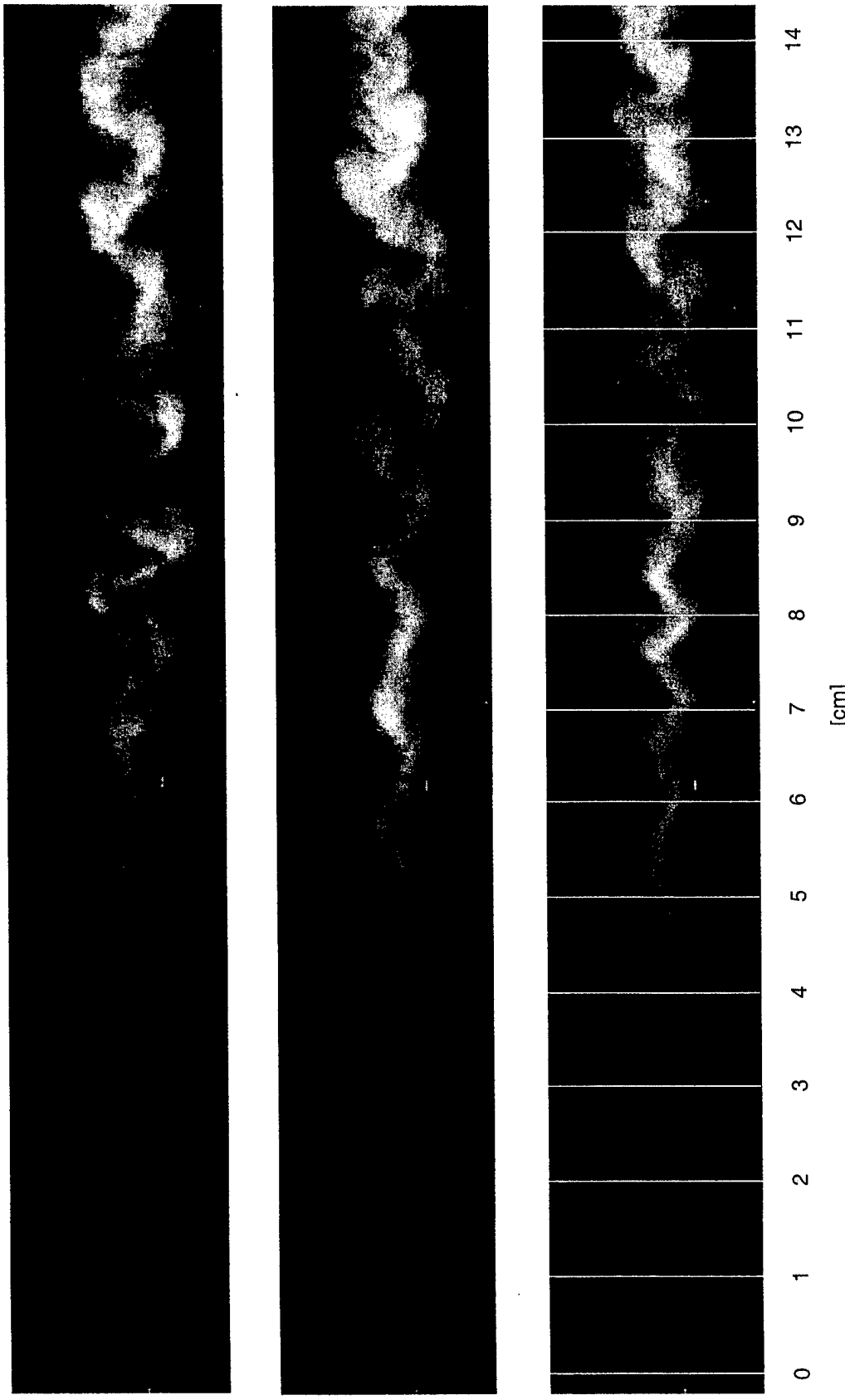


Figure 9. Typical instantaneous PLMS images for the Mach 3 wake, showing dramatically different large scale structure than for the Mach 2 wake (compare with figure 8). In this case, the PLMS signal remains extremely low until $x \approx 3.5$ cm, presumably due to reduced mixing between slot jet and free stream.

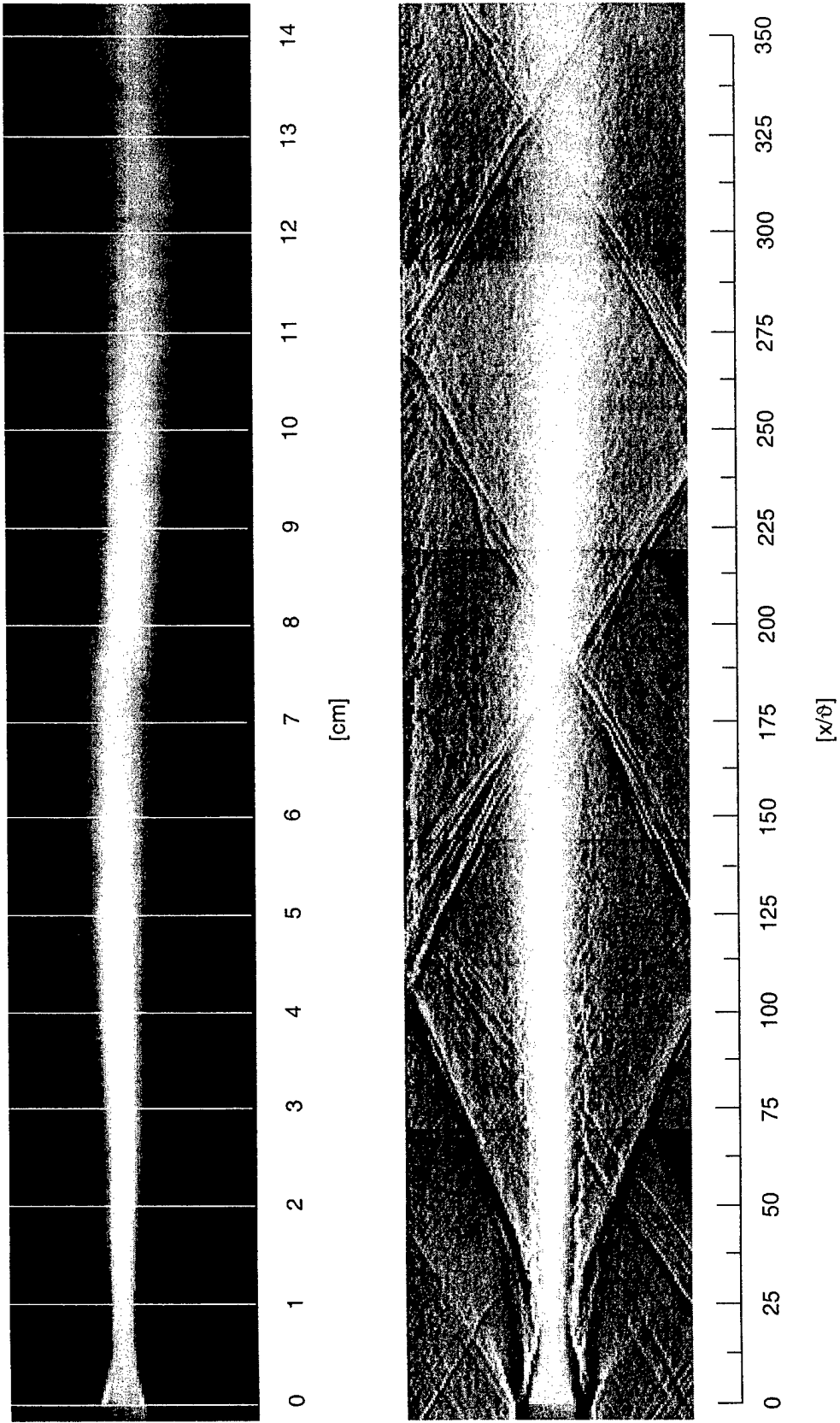


Figure 10. Ensemble-averaged PLMS image for the Mach 2 wake (*top*) and instantaneous shadowgraph image showing resulting wave structure (for parallel sidewalls) with mean PLMS image superimposed (*bottom*). Note expansion waves, recompression (shock) waves, and wall boundary layer. Scales show absolute downstream locations (cm) and corresponding relative downstream locations (x/θ) for the Mach 2 wake.

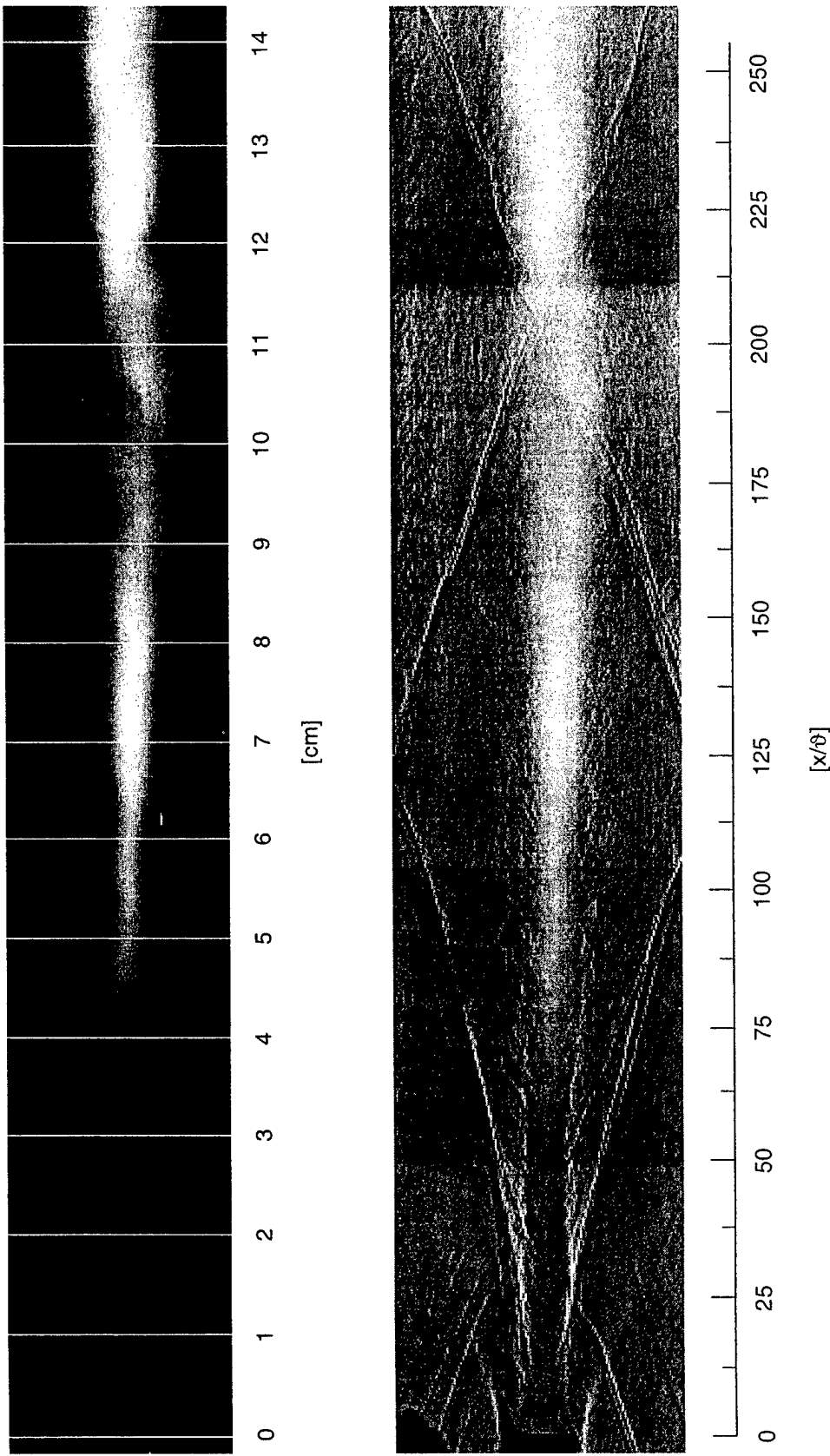


Figure 11. Ensemble-averaged PLMS image for the Mach 3 wake (*top*) and instantaneous shadowgraph image (for parallel sidewalls) with mean PLMS superimposed (*bottom*). The shallower wave angles cause the reflected waves to intersect the wake further downstream than in the Mach 2 case in figure 12. Scales show absolute downstream locations (cm) and corresponding relative downstream locations (x/θ) for the Mach 3 wake.

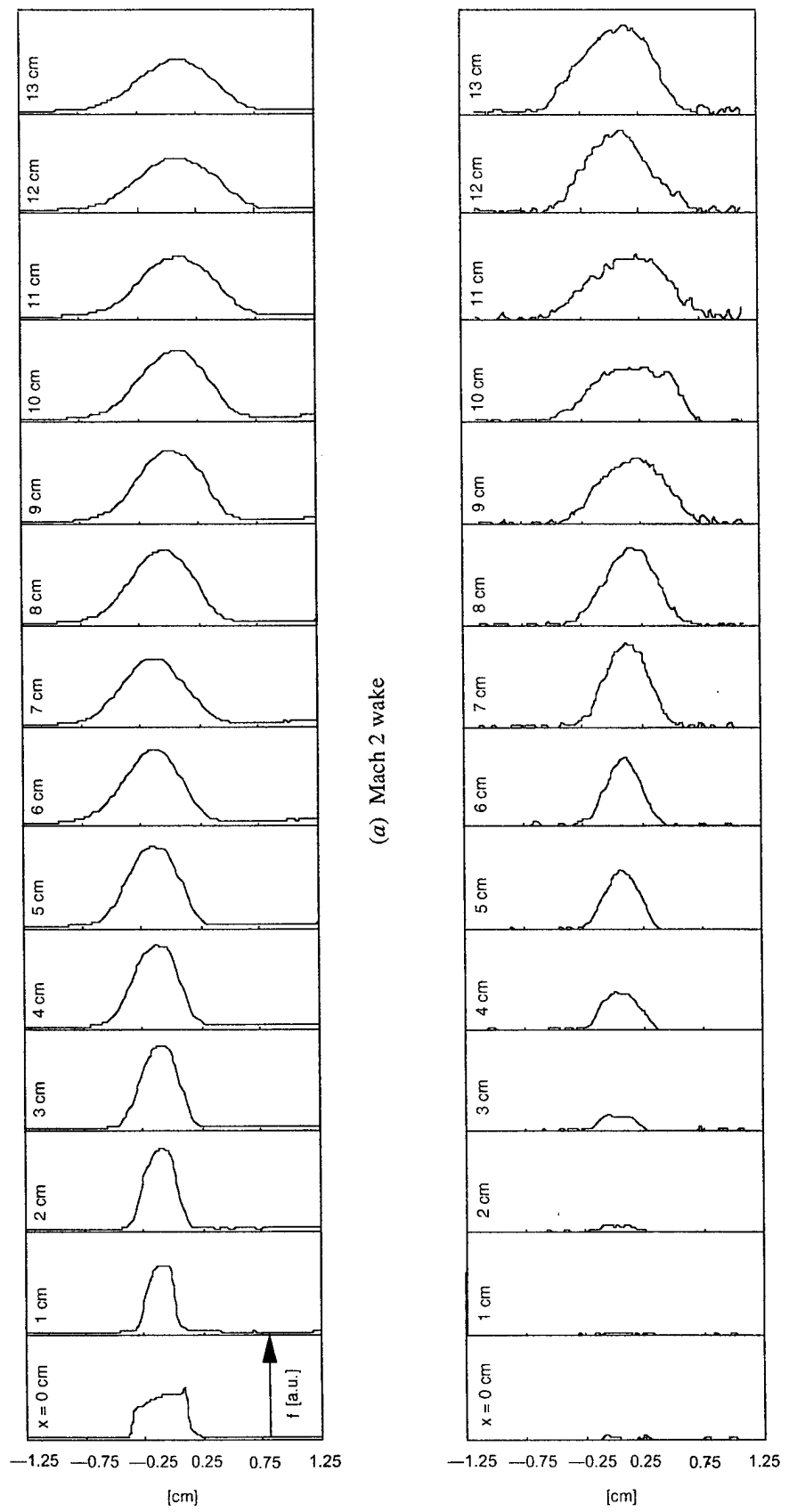


Figure 12. Ensemble-averaged PLMS intensity profiles at various downstream locations for (a) Mach 2 and (b) Mach 3 wakes. Compare absolute downstream locations with corresponding PLMS and shadowgraph images in Figs. 10 and 11. These profiles were Gauss fitted to obtain visual thickness ($\delta_{1/2}$)_{wir}.

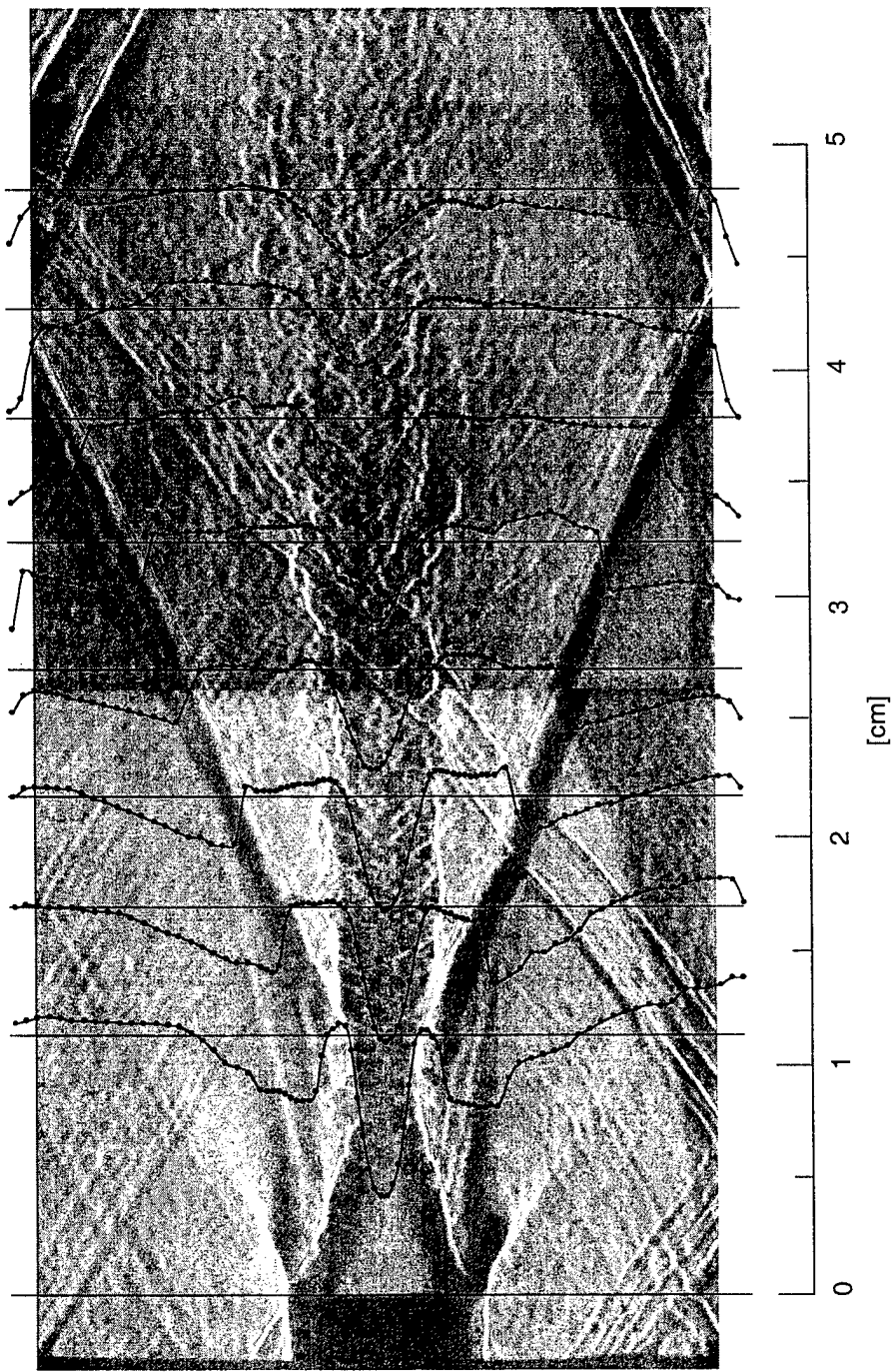
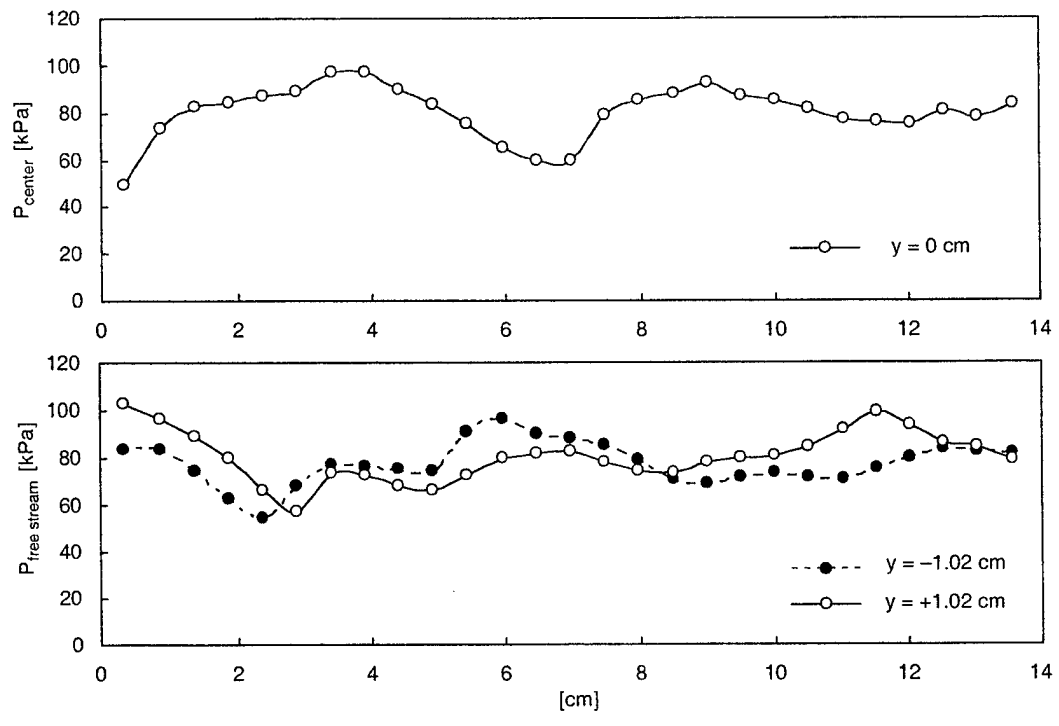
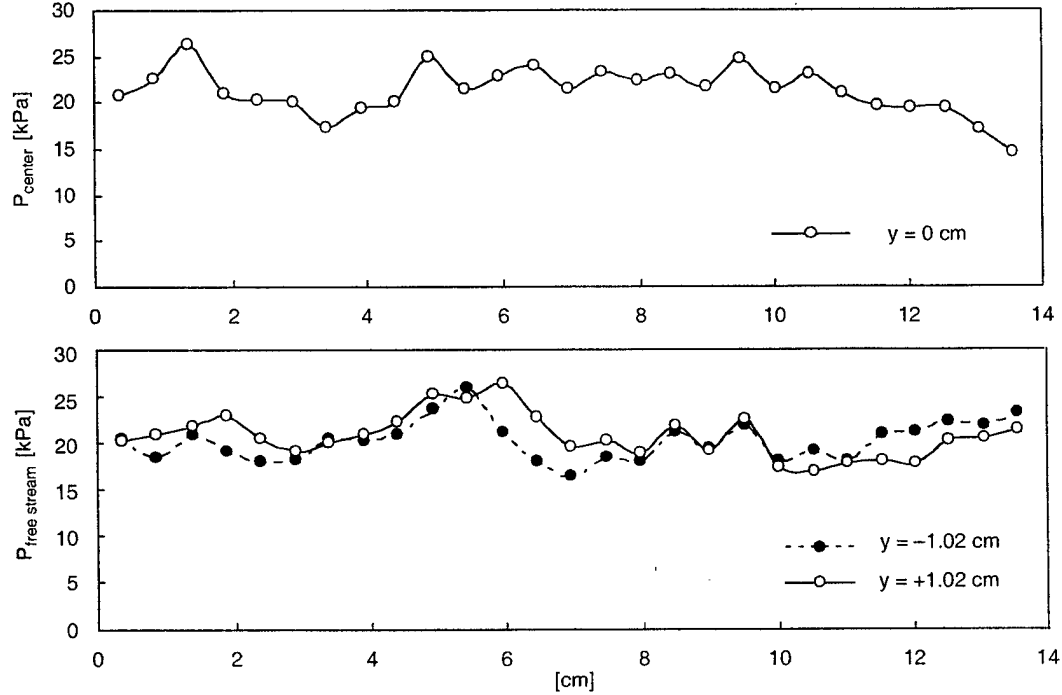


Figure 13. Total pressure profiles measured at several downstream locations, superimposed on shadowgraph image for the Mach 2 wake. Note that these profiles coincide well with the wave patterns of the supersonic bluff-body wake.



(a) Mach 2 wake



(b) Mach 3 wake

Figure 14. Measured static pressure along test section centerline (*top*) and along two off-centerline positions (*bottom*), showing variations in pressure due to wave reflections for (a) Mach 2 and (b) Mach 3 wakes.

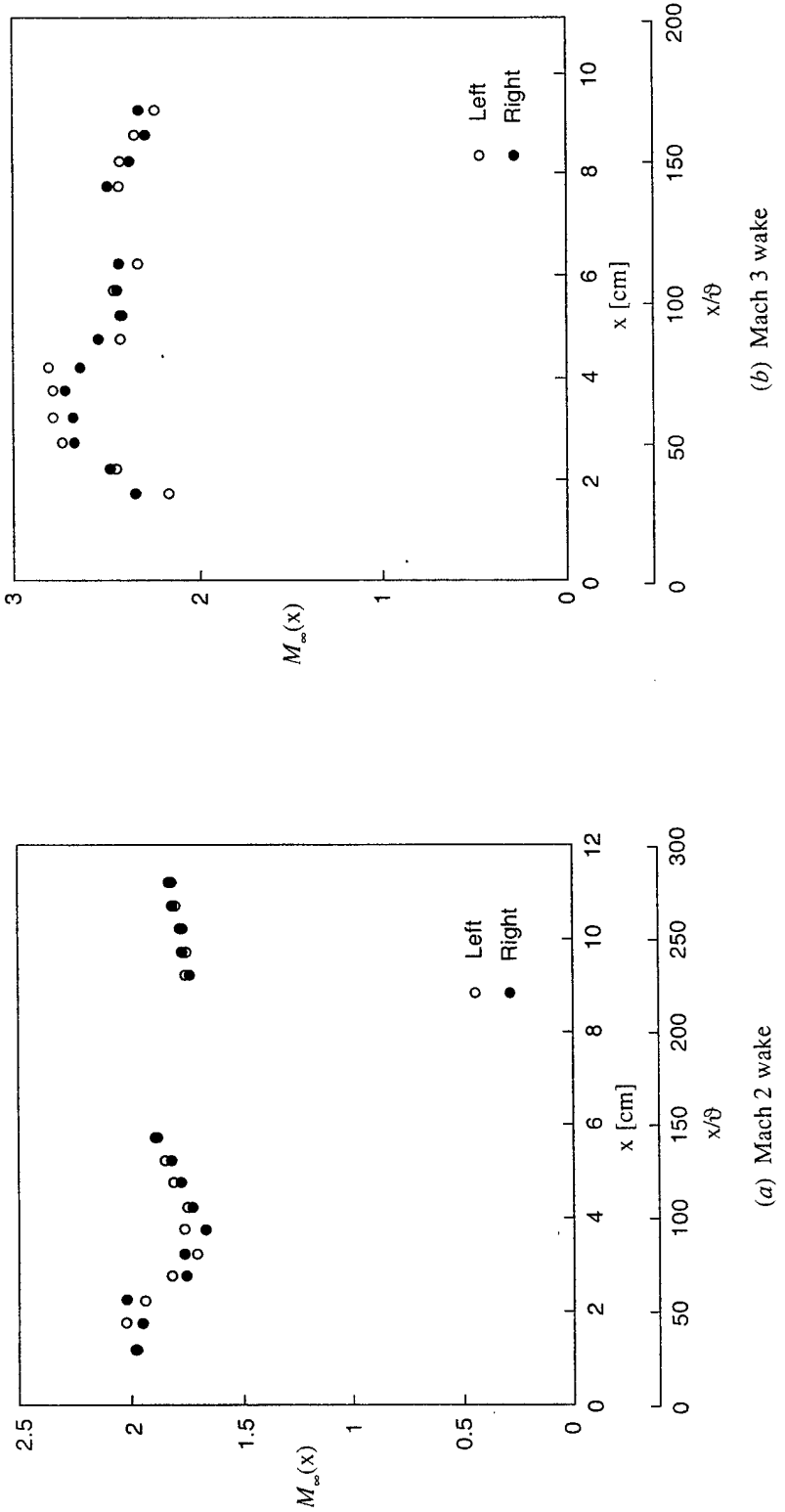


Figure 15. Free stream Mach number $M_{\infty}(x)$ outside the wake for (a) Mach 2 and (b) Mach 3 wakes.

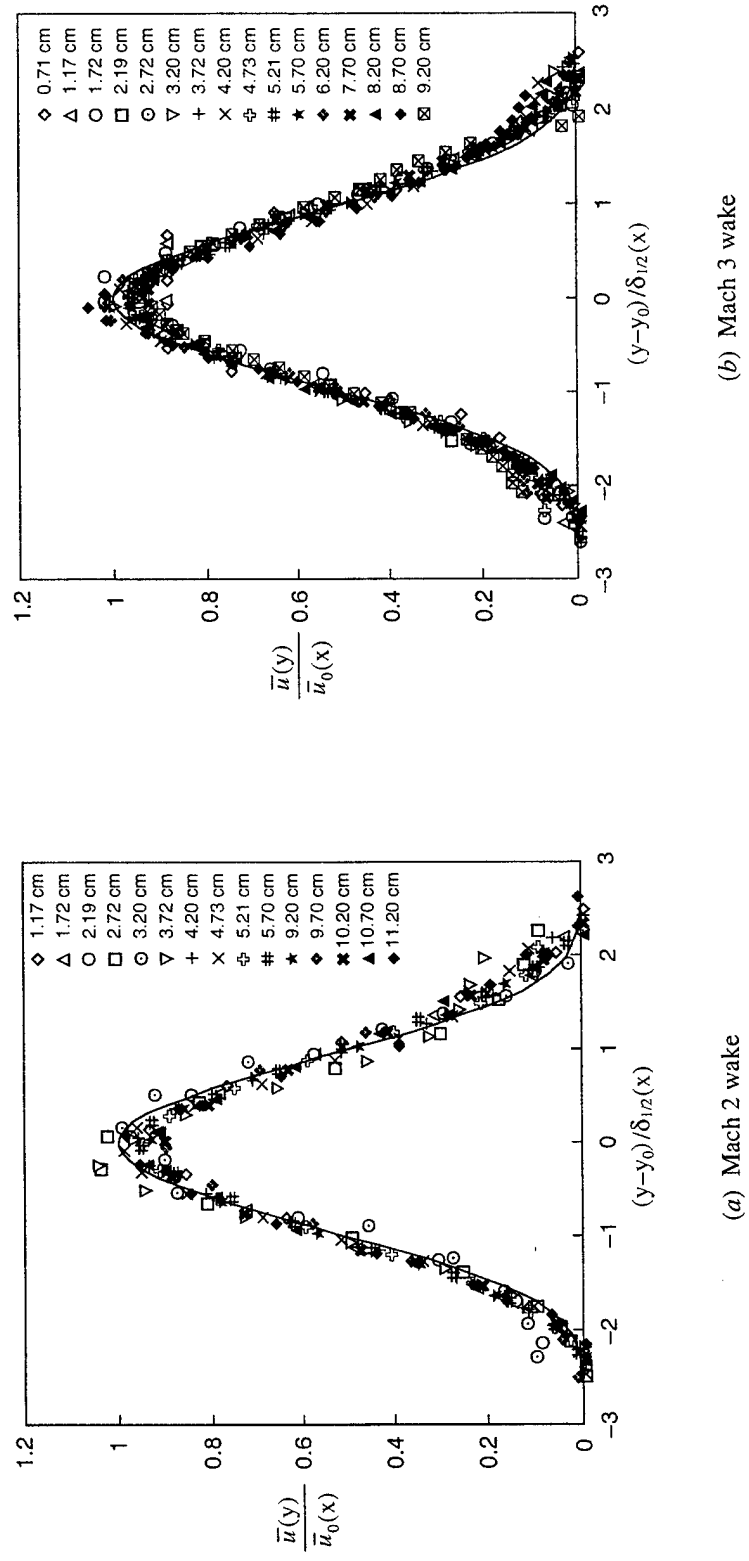


Figure 16. Similarity of measured mean streamwise velocity profiles for (a) Mach 2 and (b) Mach 3 wakes, showing good agreement of profile shapes at all downstream locations. Solid lines indicate the incompressible wake profile shape reported by Wygnanski *et al.* (1986).

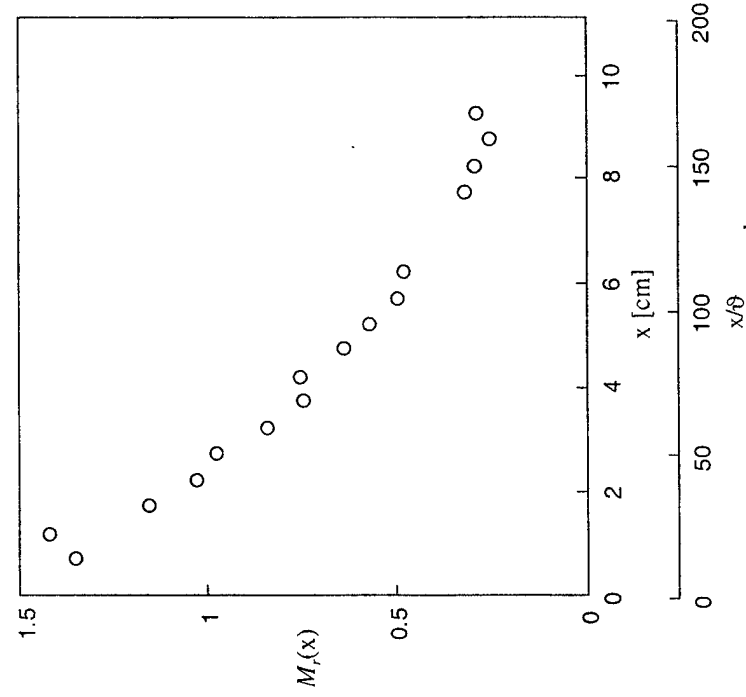
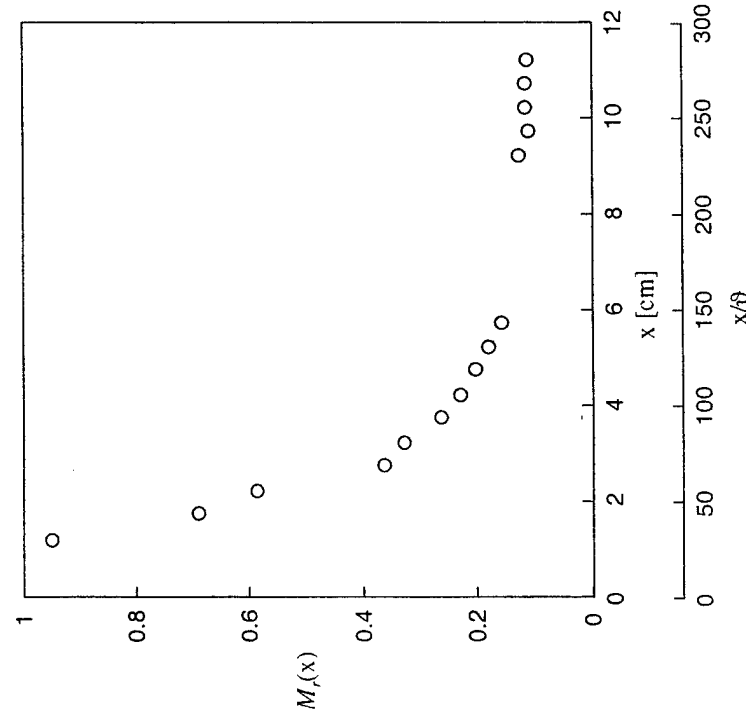


Figure 17. Relative Mach number $M_r(x)$ for (a) Mach 2 and (b) Mach 3 wakes. Note that, over the entire range of downstream locations considered for the Mach 3 wake, the relative Mach number exceeds the value 0.2 at which supersonic mixing layer studies suggest significant effects of compressibility.

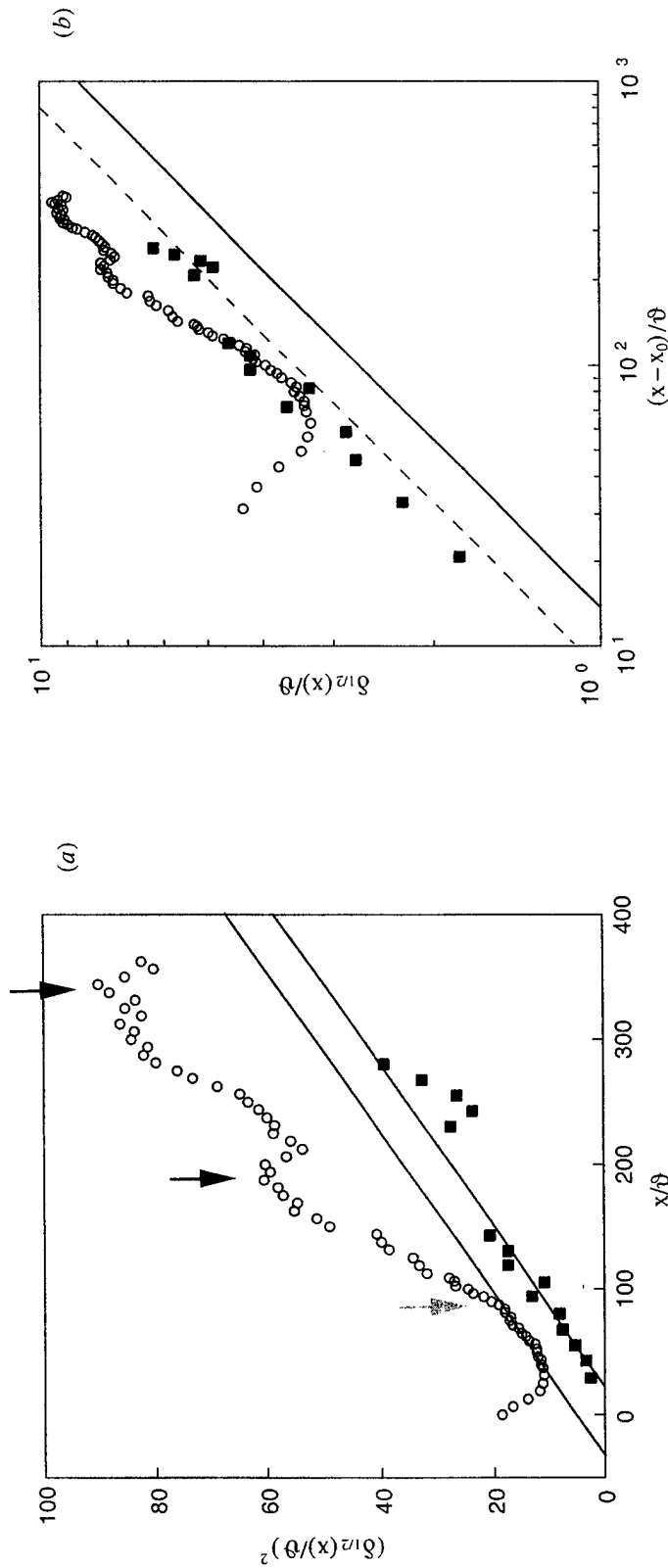


Figure 18. (a) Measured flow width $\delta_{1/2}(x)$ for the Mach 2 wake from mean PLMS intensity profiles (visual thickness) in Fig. 12a (circles) and from mean velocity profiles (velocity thickness) in Fig. 16a (squares). Straight lines show $(\delta/\delta) \sim (x/\delta)^{1/2}$ scalings, and allow virtual origins x_0 and scaling constants c_8 to be determined. Two peaks in the visual thickness indicated by black arrows near $(x/\delta) = 180$ and 330 coincide with locations of recompression wave intersections in Fig. 10. Gray arrow near $(x/\delta) = 90$ indicates location where leading characteristic of expansion wave intersects wake. (b) Flow widths $\delta_{1/2}(x)$ in log-log form, with lines indicating 1/2 power-law scaling for values of the near-field scaling constant c_8 from forced incompressible wakes (solid line) and unforced incompressible wakes (dashed line) of Wygnanski *et al.* (1986).

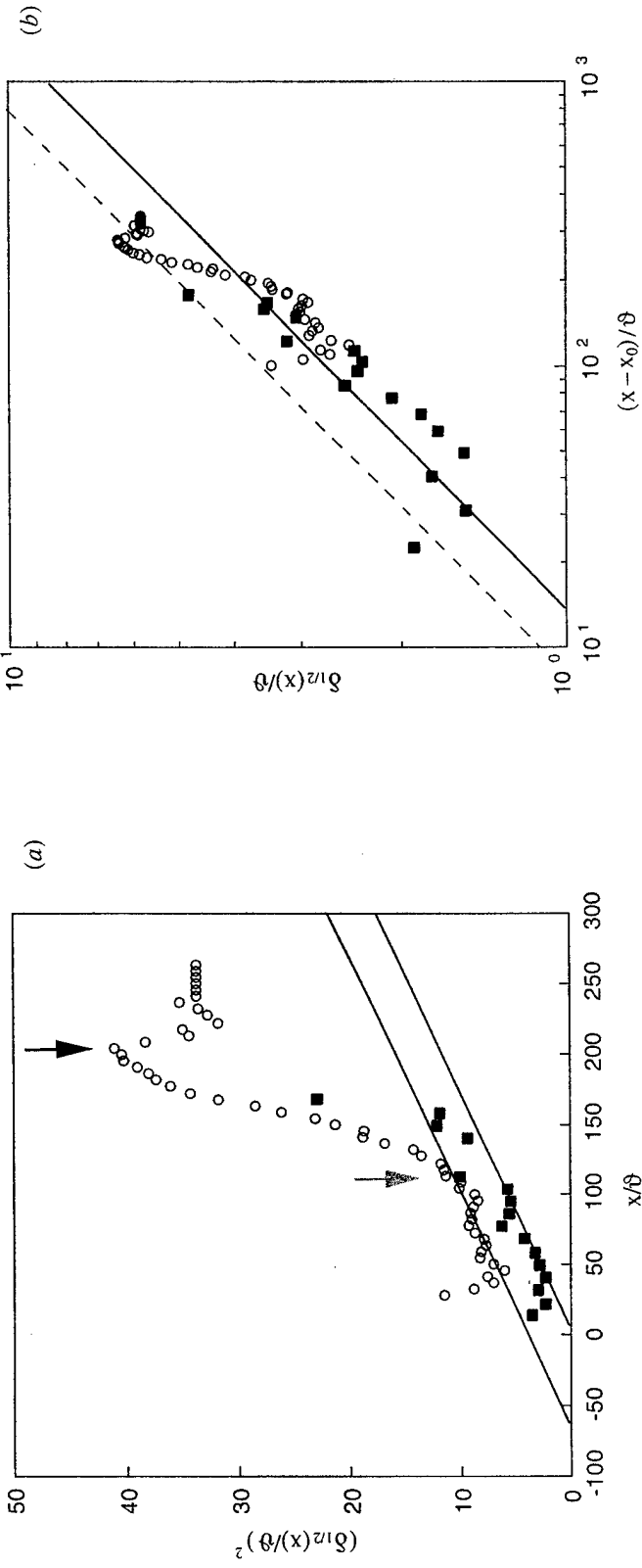


Figure 19. (a) Measured flow width $\delta_{1/2}(x)$ for the Mach 3 wake from mean PLMS intensity profiles (visual thickness) in Fig. 12b (*circles*) and from mean velocity profiles (velocity thickness) in Fig. 16b (*squares*). Straight lines show $(\delta/\delta) \sim (x/\delta)^{1/2}$ scalings. Peak visual thickness indicated by a black arrow near $(x/\delta) = 200$ coincides with location of recompression wave intersection in Fig. 11, and gray arrow at $(x/\delta) = 110$ indicates where leading characteristic of expansion wave intersects wake. (b) Flow widths $\delta_{1/2}(x)$ in log-log form, with lines indicating 1/2 power-law scaling for values of the near-field scaling constant c_8 for forced incompressible wakes (*solid line*) and unforced incompressible wakes (*dashed line*) of Wygnanski *et al.* (1986).

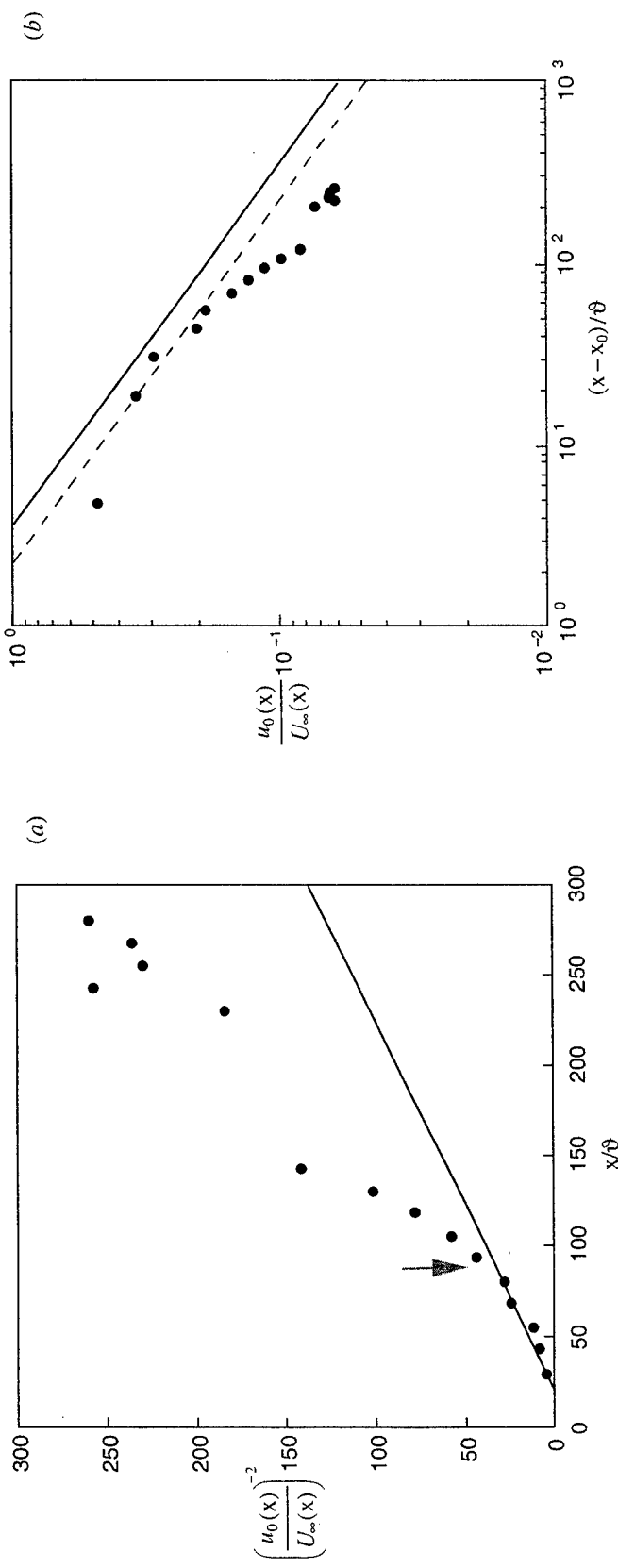


Figure 20. (a) Wake centerline defect velocity $u_0(x)$ for the Mach 2 wake from velocity profiles in Fig 16a obtained from pressure profiles. Straight line indicates $(u_0/U_\infty) \sim (x/\theta)^{1/2}$ scalings, allowing virtual origin and scaling constant c_u to be determined. Gray arrow indicates where leading characteristic of expansion wave intersects the wake. (b) Wake centerline defect velocity $u_0(x)$ in log-log form, with lines indicating $-1/2$ power-law scaling for values of the constant c_u for the forced incompressible wakes (*solid line*) and unforced incompressible wakes (*dashed line*) of Wygnanski *et al.* (1986).

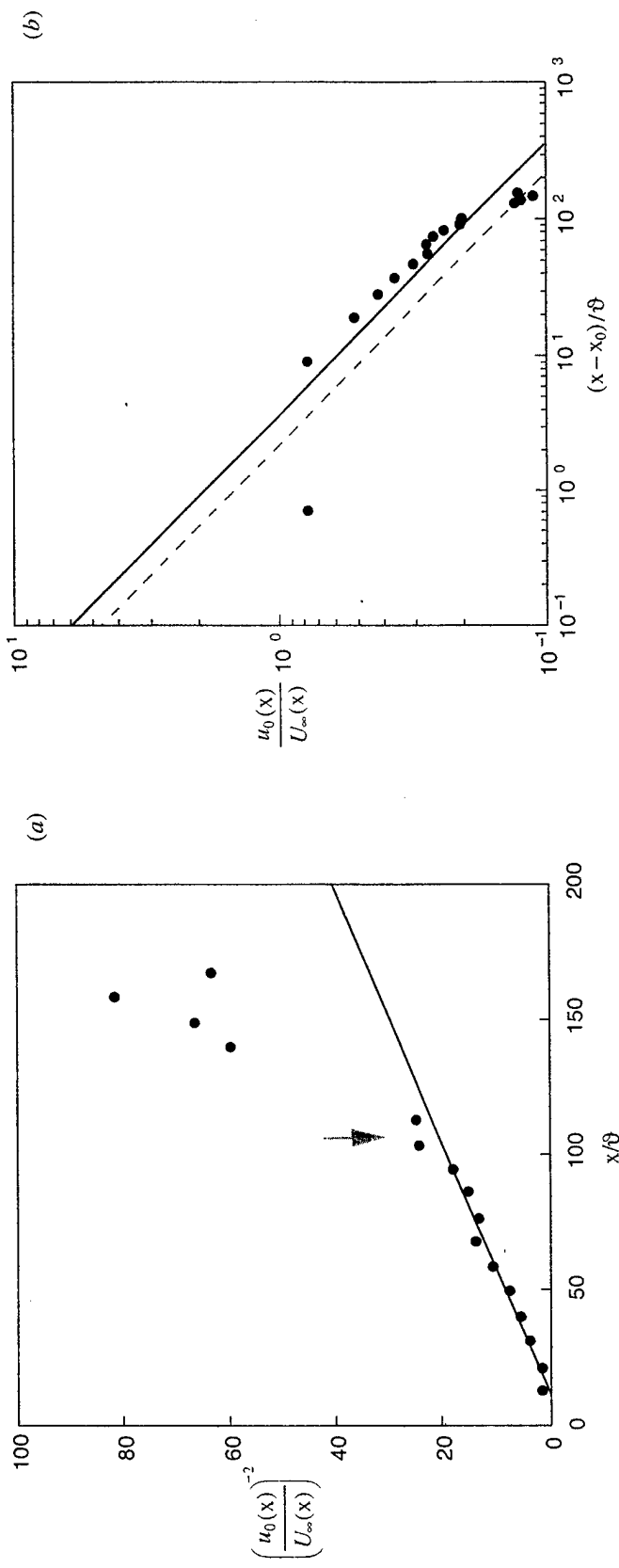


Figure 21. (a) Wake centerline defect velocity $u_0(x)$ for the Mach 3 wake from velocity profiles in Fig 16b obtained from pressure profiles. Straight line indicates $(u/U_\infty) \sim (x/\delta)^{-1/2}$ scalings. Gray arrow indicates where leading characteristic of expansion wave intersects the wake. (b) Wake centerline defect velocity $u_0(x)$ in log-log form, with lines indicating $-1/2$ power-law scaling for values of the constant c_n for the forced incompressible wakes (*solid line*) of Wygnanski *et al.* (1986) and unforced incompressible wakes (*dashed line*) of Wygnanski *et al.* (1986).

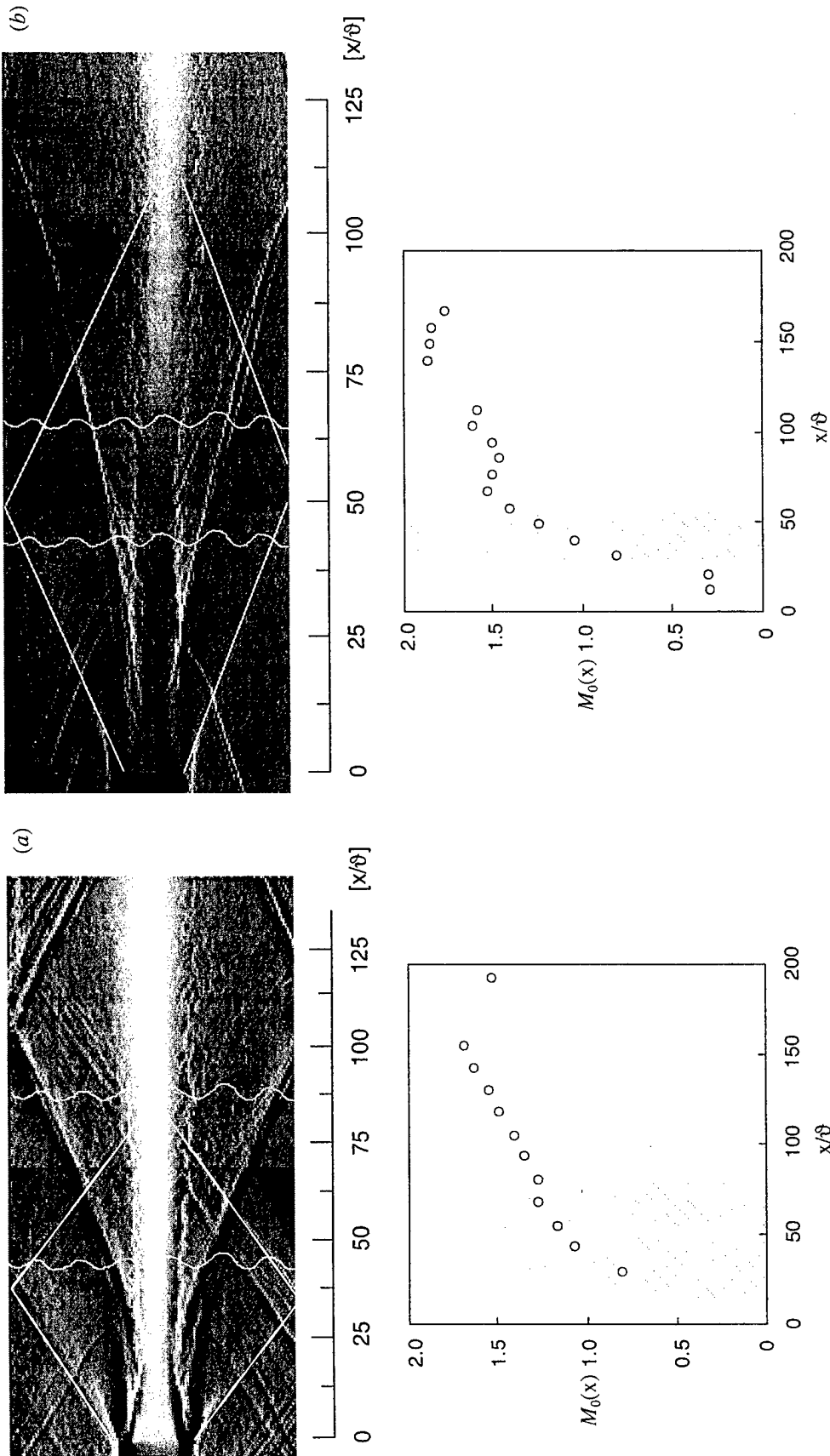


Figure 22. Feedback mechanism believed responsible for change from forced scaling constant c_8 in Mach 2 wake to unforced scaling constant in Mach 3 wake, showing shadowgraph image for (a) Mach 2 and (b) Mach 3 wakes. Note white lines in the pictures that indicate leading characteristics of expansion wave, and region where centerline Mach number changes from subsonic and supersonic. When expansion wave intersection with wake occurs where the local average centerline Mach number $M_0(x)$ is sufficiently close to subsonic as shown in the bottom figures (shaded), then pressure variations produced by the interaction can propagate upstream and force separation at the bluff body, producing a forced wake flow in the Mach 2 wake and an unforced wake in the Mach 3 wake.

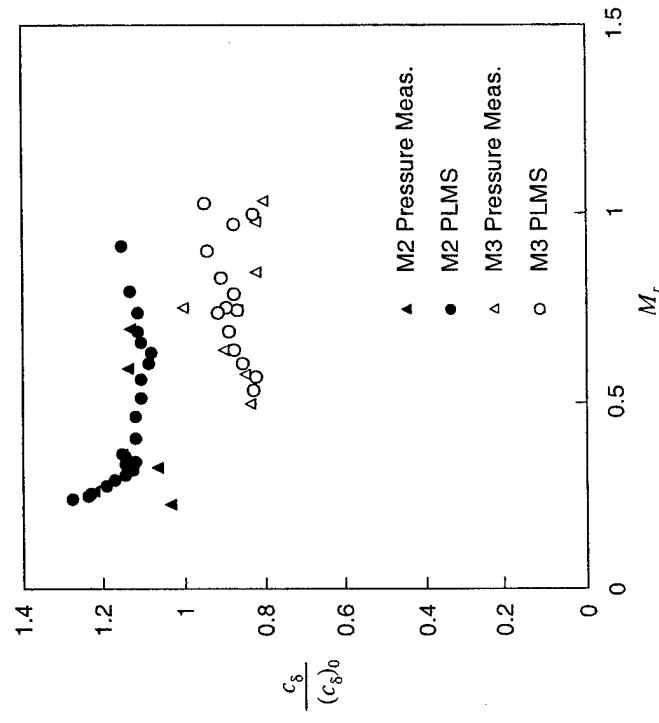


Figure 23. Plot indicating growth reduction of the supersonic planar turbulent bluff-body wake obtained from the current investigations, including PLMS, and pressure measurements, against M_r , showing the effects of the compressibility. Note that the width of the incompressible wake $\delta_{1/2}(M_r = 0)$ was determined by using the values of scaling constants of Wygnanski *et al.* (1986) for the unforced wake.

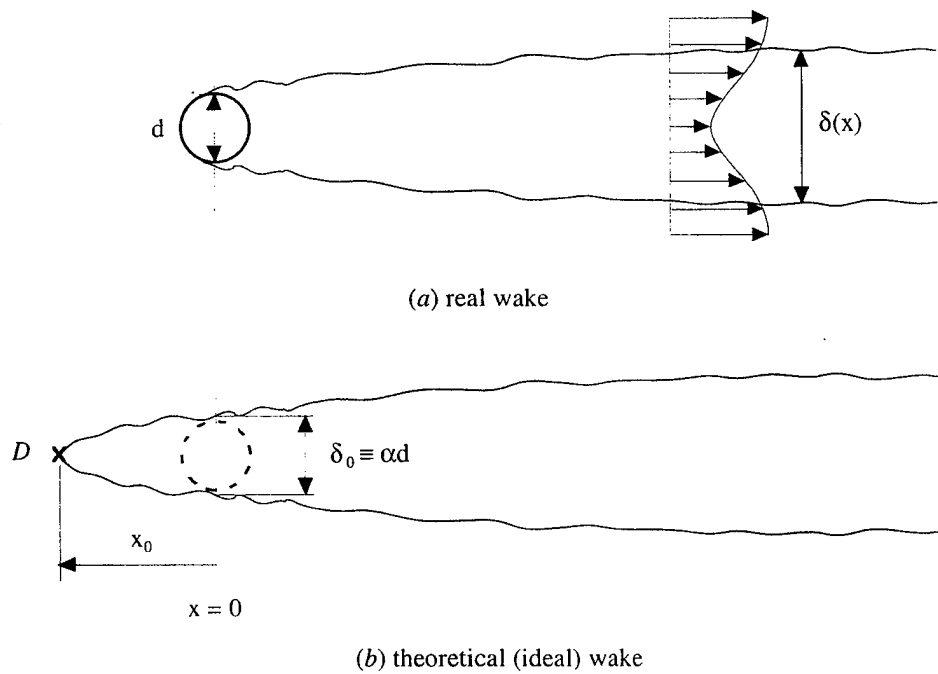
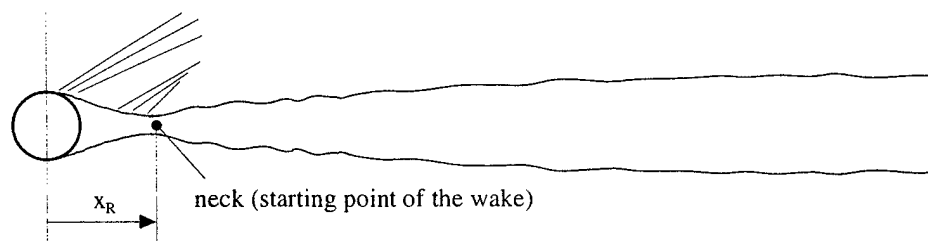
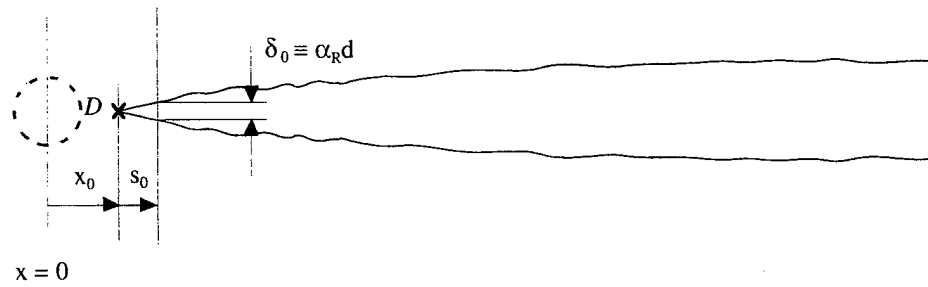


Figure A.1. Schematics of the incompressible planar turbulent wake, showing the concept of the virtual origin x_0 . Shown are (a) the actual wake produced by a bluff body, and (b) the ideal wake produced by equivalent point singularity.



(a) real wake



(b) theoretical (ideal) wake

Figure A.2. Schematics of the compressible planar turbulent wake, showing the major differences of the description of the virtual origin x_0 from the incompressible case, due to the existence of the recompression region.